Exploring the sarcoma immune landscape

Oost, S. van

4

Multimodal profiling of chordoma immunity reveals distinct immune contextures

S. van Oost, D.M. Meijer, M.E. IJsselsteijn, J. Roelands, B. van den Akker, R. van der Breggen, I.H. Briaire-de Bruijn, M. van der Ploeg, P.M. Wijers-Koster, S.B. Polak, W.C. Peul, R.J.P. van der Wal, N.F.C.C. de Miranda, and J.V.M.G. Bovée

Journal for ImmunoTherapy of Cancer **2024, 12(1).**

ABSTRACT

Chordomas are rare cancers from the axial skeleton which present a challenging clinical management with limited treatment options due to their anatomical location. In recent years, a few clinical trials demonstrated that chordomas can respond to immunotherapy. However, an in-depth portrayal of chordoma immunity and its association with clinical parameters is still lacking.

We present a comprehensive characterisation of immunological features of 76 chordomas through application of a multimodal approach. Transcriptomic profiling of 20 chordomas was performed to inform on the activity of immune-related genes through the immunologic constant of rejection (ICR) signature. Multidimensional immunophenotyping through imaging mass cytometry was applied to provide insights in the different immune contextures of 32 chordomas. T cell infiltration was further evaluated in all 76 patients by means of multispectral immunofluorescence and then associated with clinical parameters through univariate and multivariate cox proportional hazard models as well as Kaplan-Meier estimates. Moreover, distinct expression patterns of Human Leukocyte Antigen (HLA) class I were assessed by immunohistochemical staining in all 76 patients. Finally, clonal enrichment of the T cell receptor (TCR) was sought through profiling of the variable region of *TCRB* locus of 24 patients.

Chordomas generally presented an immune “hot” microenvironment in comparison to other sarcomas, as indicated by the ICR transcriptional signature. We identified two distinct groups of chordomas based on T cell infiltration which were independent from clinical parameters. The highly infiltrated group was further characterised by high dendritic cell infiltration and the presence of multicellular immune aggregates in tumours, whereas low T cell infiltration was associated with lower overall cell densities of immune and stromal cells. Interestingly, patients with higher T cell infiltration displayed a more pronounced clonal enrichment of the TCR repertoire compared to those with low T cell counts. Furthermore, we observed that the majority of chordomas maintained HLA class I expression.

Our findings shed light on the natural immunity against chordomas through the identification of distinct immune contextures. Understanding their immune landscape could guide the development and application of immunotherapies in a tailored manner, ultimately leading to an improved clinical outcome for chordoma patients.

INTRODUCTION

Chordomas are cancers displaying notochordal differentiation that arise predominantly in the axial skeleton at the skull base, the craniocervical and mobile spine, the sacrum, and, occasionally, at extra-axial areas (1). General treatment for chordomas consists of surgical resection and/or (neo-)adjuvant proton beam radiation. Since most chordomas are indolent tumours, chemotherapy is considered ineffective for the treatment of this disease (2). The clinical management of chordoma patients is complicated by the anatomical location of the tumours, their often late detection, as well as treatment-related morbidities (2, 3). Aiming at a gross total or en bloc resection involves sacrifice of neurovascular structures with permanent neurological disabilities. As such, disease recurrence is common after treatment and 30-40% of chordoma patients develop metastases (4). The overall 5-year survival following diagnosis is around 67% and there are currently no curative therapies for chordoma patients with advanced disease (1, 5). This reinforces the need for innovative treatments as local recurrences and distant metastases persist.

Recent findings have provided evidence for the presence of conspicuous immune cell infiltration in chordomas (6, 7) and, encouragingly, clinical responses of chordoma patients to checkpoint blockade immunotherapy targeting CTLA-4 and/or the PD-1/PD-L1 axis have been reported (8-12). This is an intriguing observation as chordomas display a low mutational burden and are, instead, affected by gross chromosomal alterations (13-15). Furthermore, PD-L1 expression is rarely encountered in sarcomas, including chordomas (16-18). Instead, the presence of pre-existing anti-tumour immune responses perceived by the infiltration of cytotoxic T cells in the tumour tissue or by the presence of tertiary lymphoid structures appear to inform on the sensitivity of soft tissue sarcomas to immune checkpoint blockade (19, 20). So far, whether tertiary lymphoid structures are predictive of responsiveness to immune checkpoint blockade has not been investigated in chordomas.

An in-depth immunological characterisation of chordomas and their association with clinical parameters is currently lacking. Here, we applied transcriptomic profiling and multidimensional immunophenotyping by imaging mass cytometry and multispectral immunofluorescence to resolve the immune landscape of chordomas. Chordomas presented hallmarks of anti-tumour immunity and were considered immune “hot” in comparison with other sarcomas. Within our cohort, we identified groups of chordomas with distinct immune contextures, independent from any clinical parameter. Our findings

support the rational utilisation of immunotherapeutic approaches, tailored to target these distinct microenvironments in chordoma.

METHODS

Patient samples

Formalin-fixed paraffin embedded (FFPE) and snap-frozen tissue material was initially collected for 43 and 24 chordomas respectively from 32 patients, followed by a second expansion cohort containing FFPE material of an additional 53 patients. Regions of interest (ROIs) representative for the tumour's immune microenvironment were selected on Haematoxylin & Eosin (H&E) sections of decalcified FFPE tissue by a bone and soft tissue tumour pathologist (JVMGB). These ROIs were then used to create tissue micro arrays (TMAs) using a TMA Master (3DHISTECH). These TMAs were holding 2-4 cores of 1.6 mm in diameter per tumour, dependent on the source of the material or the morphology of the tumour (two cores: biopsy; three cores: resection/excision etc; four cores: heterogeneous morphology, or separate areas of dedifferentiation). As controls and for orientation purposes, each TMA contained three cores tonsil and three cores placenta, either decalcified with EDTA or formic acid or non-decalcified.

RNA sequencing data

RNA was isolated from snap-frozen tissue from 20 primary tumours with TRIzol and Isopropanol/Ethanol. In addition, RNA sequencing data from primary tumours of osteosarcoma patients (n = 7; GSE237033), chondrosarcoma patients (n = 9), undifferentiated soft tissue sarcoma patients (n = 13), and myxofibrosarcoma patients (n = 10) was taken along as a means of comparison. RNA purification was performed with the RNeasy kit which included treatment with DNase. Paired-end 150 base pair (bp) reads were created on a NovaSeq6000 Illumina at GenomeScan (Leiden, The Netherlands). The sequencing data was processed with the RNA-seq BioWDL pipeline from the SASC with default settings (BioWDL Github, LUMC, The Netherlands). Alignment of the 150bp reads to hg38 was performed with STAR, after which the gene expression was quantified with HTSeq-count (21). The processed sequencing data was stored as a matrix containing the counts per gene per sample.

Gene expression analysis

Normalisation and exploratory analysis of the RNA sequencing data was performed in R (v.4.0.2) by using DESeq2 (v. 1.30.1). BiomaRt (R, v.2.46.3)

was used to translate the ensemble IDs to known protein coding genes. The most variably expressed genes were determined by calculating the variance per gene across all samples. The immunologic constant of rejection (ICR) gene signature was used to describe the activity state immune microenvironment and to identify distinct immune-related clusters (Th1-related markers: *IFNG*, *STAT1*, *IL12B*, *IRF1*, *TBX21*; CD8+ T cells: *CD8A*, *CD8B*; Immune effector molecules: *GZMA*, *GZMB*, *GZMH*, *PRF1*, *GNLY*; Chemokine ligands: *CXCL9*, *CXCL10*, *CCL5*; Immune suppressive molecules: *IDO1*, *PDCD1*, *CD274*, *CTLA4*, *FOXP3*) (22). The mean of the log2 normalised expression of these 20 genes was used to attribute an ICR "score" to each sample for comparison between the sarcoma subtypes, which was visualised with ggplot2 (R, v.3.3.6). For both the heatmaps in **figure 1**, a Z-Score was calculated per gene to visualise the transcriptional profile of the samples by using the Ward variance method with ComplexHeatmap (R, v.2.11.1). Differential gene expression analysis was performed with DESeq2 comparing chordomas to all other sarcomas. Genes were considered differentially expressed when the log2 fold change was above 2 and the adjusted *P* value was below 0.01. Immune-related genes were selected for visualisation in the enhanced volcano plot and additional boxplots. For visualisation purposes, the axes of the enhanced volcano plot were manually adjusted as follows: log2 fold change (x-axis) was set between -10 and 10, and the -log10 adjusted *P* (y-axis) was set to a maximum of 100.

Imaging mass cytometry

Conjugation of BSA-free antibodies and immunodetection with a 40-marker tumour immune microenvironment panel (**supplemental table 1**) was performed as previously described (23). In brief, four-µm sections of the created TMAs were deparaffinised and rehydrated, after which heat-induced antigen retrieval was performed in 1x low pH antigen retrieval solution (pH6, Thermo Fisher Scientific). Subsequently, the first batch of primary antibodies were incubated overnight at 4 °C. After washing in PBS supplemented with 1% BSA and 0.05% Tween, conjugated anti-mouse and anti-rabbit antibodies were incubated for one hour at room temperature. Next, the sections were incubated with the second batch of primary antibodies for five hours at room temperature, followed by an overnight incubation at 4 °C with the final batch of primary antibodies. To finish, 1.25 µM of the DNA intercalator Iridium (Fluidigm) was incubated for five minutes to stain DNA, after which the sections were washed, air-dried and stored at room temperature. ROIs of 1000x1000 µm were selected with consecutive H&E slides and ablated by using a Hyperion mass cytometry imaging system (Fluidigm) at the Flow Core Facility (LUMC,

Leiden) within a month after staining. The imaging data was acquired with CyTOF Software (v.7.0), visually inspected and then exported with MCD Viewer (v.1.0.5). In the end, 127 tumour ROIs were successfully ablated and analysed.

Imaging mass cytometry analysis

To correct for variability in signal-to-noise ratios between FFPE sections, the signal intensity of the generated images was normalised at pixel levels by using Matlab (v.R2021a), after which the images were binarised using semi-automated background removal in Ilastik (v.1.3.3) as described previously (23). Probability masks were generated in Ilastik by using a multicoloured image including the DNA channel, CD45 channel, Keratin channel and Vimentin channel to annotate nucleus, cytoplasm and background. Probability masks were loaded into CellProfiler (v.2.2.0) and used for creating cell segmentation masks. Next, the segmentation masks and binarised images were loaded into ImaCyte (24) to generate single cell-FCS files containing relative frequency of positive pixels for each marker, which were then used for phenotyping in CytoSplore (v.2.3.1) by sequentially utilizing Hierarchical Stochastic Neighbour Embedding (H-SNE) and t-distributed Stochastic Neighbour Embedding (t-SNE). Identified cell phenotypes were loaded into ImaCyte together with the segmentation masks and binarised images, which allows the mapping of the phenotypes back onto the images. Phenotypes per image were extracted to calculate the mean cell density per mm^2 for every sample (one image = one mm^2). An overview of the lineage markers used for phenotype identification is listed in **supplemental table 2**. Patients were clustered into two groups based on the Z-Score normalised mean cell densities per mm^2 of all five identified T cell phenotypes by using the Ward variance method with ComplexHeatmap. Ggplot2 was used to visualise the mean cell densities and to compare them between both T cell groups. For statistical testing, a two-sided student's t-test was performed followed by a Benjamini-Hochberg FDR correction. In addition, an overview heatmap containing all identified phenotypes in the microenvironment of chordomas was visualised with ComplexHeatmap.

Spatial interaction analysis

After phenotype calling, a spatial interaction analysis was performed with ImaCyte for all imaged samples, comparing T cell low with T cell high chordomas. ImaCyte utilises a 1000-iteration permutation test which calculates a Z-Score for the interaction between adjacent cells. However, permutation testing does not adjust for overabundant cell types, such as tumour cells, and is therefore not able to identify meaningful interactions for tumour cells. Because

of the range of the calculated Z-Scores, interactions with a Z-Score below 10 were considered not significant and therefore removed for visualisation only. If an interaction Z-Score was higher than 10 in one group and lower than 10 in the other group, this interaction was considered significant for one group. When both Z-Scores were higher than 10, this interaction would be considered significant in both groups. A comparative interaction heatmap between all phenotypes excluding tumour cells was visualised with ggplot2.

Multispectral immunofluorescent imaging of T cells

A T cell panel comprising five markers for five channels was generated for imaging with a Vectra (Akoya Biosciences) as previously described (25) for validation purposes. This panel included FoxP3 (236A/E7, 1:1000, Invitrogen, 14-4777-82), CD8α (D8A8Y, 1:100, Cell Signaling Technology, #85336), CD3ε (EP449E, 1:50, Abcam, ab52959), pan-cytokeratin (AE-1/AE-3 & C11, both 1:50, Novus & Santa Cruz, NBP2-33200AF647 & SC-8018) and Ki-67 (8D5, 1:200, Cell Signaling Technology, #9449) and DAPI as a nuclear staining. In short, slides were deparaffinised and incubated in 0.3% H_2O_2 in methanol for 20 minutes to block endogenous peroxidase. After antigen retrieval in citrate (pH 6.0), slides were incubated for 30 minutes with SuperBlock™ Blocking Buffer (ThermoFisher Scientific). Next, slides were incubated with primary antibody (FoxP3) for one hour at room temperature and subsequently with BrightVision DPVO-HRP (Immunologic) for 30 min at room temperature. Opal 520 reagent (Akoya Bioscience) was diluted in Opal amplification diluent and then added to the slides for one hour at room temperature, after which the slides were heated in citrate buffer (pH 6.0) for 15 min. The second round of primary antibodies (CD8α and Ki-67) were incubated overnight at room temperature and then stained with their respective fluorescent secondary antibodies (CF555, 1:400, Biotum and Alexa 680, 1:200, Invitrogen) for one hour at room temperature. Finally, the slides were stained with directly conjugated antibodies (CD3ε-Alexa 594 and pan-cytokeratins-Alexa 647) for 5 hours at room temperature and then mounted. All TMAs were imaged at 20x, after which the images were processed with inForm (v.2.4), which comprises background removal for each antibody by normalisation of the spectra, and analysed with QuPath (v.0.3.1). Object classification was performed by using the following classes: $CD3^+FOXP3^+$ = Regulatory T cells, $CD3^+CD8^+$ = $CD8^+$ T cells, $CD3^+$ = $CD4^+$ T cells, $CD3^+Ki\text{-}67^+$ = Proliferating T cells, CD3- = Rest. Counts per image (one image = 1 mm x 1.3 mm) were normalised per patient to counts per mm^2 tissue. Patients were divided into a T cell high and low cluster based on the unsupervised clustering of the Z-scores of all T cell phenotypes in R.

Survival analysis

For all chordoma patients, Kaplan-Meier curves for the disease-specific survival and recurrence-free survival were generated with the survminer and survival packages (R, v.0.4.9 and v.3.1-12 respectively). The disease-specific survival was considered the survival of a patient until death due to the disease, whereas the recurrence-free survival was considered the time until a patient was diagnosed with a recurrence, thereby excluding patients who did not receive surgery. Since the cohort included many censored cases, the log-rank *P* value was used to estimate the significance of the associations. Known prognostic factors such as the anatomical tumour location excluding the only extra-axial patient, age and type of treatment, surgical margin excluding patients who did not receive surgery and disease recurrence were investigated for their prognostic value, as well as the newly identified T cell infiltration groups. Univariate and multivariate analyses were performed in R according to the cox proportional hazard model. Only clinical parameters that were found significant in the univariate analysis were taken along in the multivariate analysis.

Immunohistochemical detection of HLA class I and β-2m

Immunohistochemistry was performed for the HLA class I heavy chain (HCA2, 1:1000, Nordic Bio, MUB2036P; HC10, 1:3200, Nordic Bio, MUB2037P) and β-2m (EPR21752-214, 1:4000, Abcam, ab218230) on all generated TMAs as described previously (26). Briefly, antigen retrieval was performed in citrate (pH 6.0), after which the TMA sections were pre-incubated with PBS-5% non-fat dry milk for 30 min at room temperature. Primary antibody dilutions were incubated overnight at 4 °C, after which the sections were incubated with BrightVision DPVO-HRP (Immunologic) for 30 min at room temperature. Finally, TMA sections were further developed with liquid DAB+ chromogen (Dako) for 10 min and subsequently counterstained with haematoxylin. Samples were classified as HLA class I positive, weak, or defective depending on the expression pattern of HC10 and HCA2 in the tissue and the contrast between the expression of the tumour cells and the immune cells. Tumours were classified as defective if one or more of the HLA class I antibodies were negative in the tumour cells. The distribution of the expression patterns among the identified T cell groups was visualised in R using ggplot2.

TCR β-chain sequencing

DNA was isolated from snap-frozen tissue from 27 chordomas from 23 patients for sequencing of the variable region of the *TCRB* locus. In brief, DNA libraries were generated with the AmpliSeq Library Kit Plus and the OncoMine TCRβ-

SR Assay following the manufacturer's instructions. Sample libraries were measured with the ION Library TaqMan Quantitation Kit and then pooled to a final concentration of 25 pM. Next, the pooled libraries were templated on ION 540 Chips with the Ion Chef System. The 80bp reads were created on an Ion GeneStudio S5 Prime Sequencing Technology at GenomeScan (Leiden). The number of clones and the Shannon diversity, a measure for clonal enrichment, were calculated in R by using productive counts only, meaning that a clone needed at least 10 plus and 10 minus counts. Because recurrences showed similar levels of TCR diversity as their respective primary tumour, we used the TCR repertoire of recurrences for three patients for which there was no frozen material of primary tumours available. Finally, the data was visualised in R using ggplot2.

RESULTS

Patient characteristics

In this study, two cohorts were established to investigate the immune microenvironment of chordomas. The first cohort included primary tumours of 32 patients and was explored using RNA sequencing (*n* = 20) and imaging mass cytometry (*n* = 32). The median age was 59 years (range 1 - 80 years) and the median follow-up time was 66 months (range 0 - 418 months). In total, the primary tumours in the cohort comprised eight skull base chordomas (25%), seven spinal chordomas (22%) and 17 sacrococcygeal chordomas (53%). The second cohort included primary tumours of an additional 53 patients. The median age of this cohort was 60 years (range 22 – 80) and the median follow-up time was 41 months (range 0 - 182). In total, this cohort comprised 17 skull base (32%), 15 spinal chordomas (28%), 20 sacrococcygeal chordomas (38%) and one extra-axial chordoma of the ribs (2%). The second cohort also comprised patients solely treated with radiotherapy, for which the treatment-naïve biopsies were used. All profiled primary tumour samples were annotated for their anatomical location as well as whether they underwent neoadjuvant radiotherapy. Further patient characteristics of both cohorts are listed in **table 1**.

Table 1. Patient characteristics of chordoma cohorts. This table contains an overview of each cohort separately as well as both cohorts combined.

Variable	First		Second		Combined	
Total patients, *n*	32		53		85	
Gender, *n* (%)						
Female	15	(46.9)	21	(39.6)	36	(42.4)
Male	17	(53.1)	32	(60.4)	49	(57.6)
Age (years), *median* (range)	59	(1-80)	60	(22-80)	60	(1-80)
Follow-up (months), *median* (range)	66	(0-418)	41	(0-182)	50	(0-418)
Anatomical location, *n* (%)[a]						
Skull base (Clivus)	8	(25.0)	17	(32.1)	25	(29.4)
Mobile spine (Craniocervical, Cervical, Thoracic, Lumbar)	7 (0, 1, 4, 2)	(21.9)	15 (3, 10, 1, 1)	(28.3)	22	(25.9)
Sacrococcygeal	17	(53.1)	20	(37.7)	27	(31.8)
Extra-axial (Costa)	-	-	1	(1.9)	1	(1.2)
Max tumour size (cm), *median* (IQR)[b]	7	(4.5)	6	(6.1)	6.1	(5.6)
Skull base (Clivus)	2.8	(0.88)	4.3	(1.5)	4	(2.5)
Mobile spine (Craniocervical, Cervical, Thoracic, Lumbar)	5.5	(3.4)	4.9	(1.4)	5	(1.7)
Sacrococcygeal	8	(4)	10.5	(3.6)	9	(3.9)
Extra-axial (Costa)	-	-	10	-	10	-
Treatment, *n* (%)						
Radiotherapy alone	-	-	11	(20.8)	11	(12.9)
Surgery alone	21	(65.6)	19	(35.8)	40	(47.1)
Surgery & radiotherapy	11	(34.4)	23	(43.4)	34	(40)
Other radiotherapy regimens, *n* (%)						
Monotherapy, conventional	-	-	1	(1.9)	1	(1.2)
Monotherapy, proton beam	-	-	9	(17)	9	(10.6)
Monotherapy, carbon ion	-	-	1	(1.9)	1	(1.2)
Sandwich, proton beam	-	-	2	(3.8)	2	(2.4)
Pre-operative radiotherapy, *n* (%)[c]						
Conventional	4	(12.5)	2	(3.8)	6	(7.1)
Proton beam	2	(6.3)	1	(1.9)	3	(3.5)
Post-operative radiotherapy, *n* (%)[c]						
Conventional	5	(15.6)	7	(13.2)	12	(14.1)
Proton beam	-	-	11	(20.8)	11	(12.9)
Patients with recurrent disease, *n* (%)[d]						
Local recurrence	16	(50)	29	(54.7)	45	(52.9)
Metastasis	6	(18.8)	14	(26.4)	20	(23.5)

[a]anatomical location of the primary tumours; [b]size was not available for 8 and 11 primary tumours in the initial and the additional cohort respectively (4 skull base and 2 mobile spine; 2 skull base, 2 mobile spine and 7 sacrococcygeal); [c]treatments regarding primary tumours; [d]Patients who experienced recurrent disease during follow-up. With the exception of 3 patients in the additional cohort, metastatic disease followed local recurrence.

Chordomas present transcriptional hallmarks of anti-cancer immunity

The transcriptomic profiles of the 20 chordomas were compared to those of osteosarcomas (*n* = 7), chondrosarcomas (*n* = 9), undifferentiated soft tissue sarcomas (USTS) (*n* = 13), and myxofibrosarcomas (*n* = 10). All chordoma samples clustered separately from the remaining sarcomas following unsupervised clustering based on the 200 genes with most variable expression among all samples (**figure 1A**). Sample clustering was largely driven by features related to the line of differentiation of the different sarcoma samples, with known chordoma-related genes such as *TBXT*, *CD24*, and several keratins enriched in the chordomas (27-29) (**figure 1A**, **supplemental table 3**). Moreover, genes associated with the extracellular matrix and adhesion related genes were enriched in chordomas and chondrosarcomas as compared to the other sarcomas (**figure 1A**, **supplemental table 3**). Interestingly, several immune-related genes, including Human Leukocyte Antigen (HLA) class I, HLA class II, *PLA2G2D* and immunoglobulin genes, were among the most variably expressed genes and were enriched in specific chordomas. Furthermore, differential gene expression analysis revealed enrichment for other immune-related genes in chordomas in comparison with the other sarcomas (**supplemental figure 1A-B**, **supplemental table 4**).

To substantiate that immune-related processes are enriched in chordomas, we evaluated the expression of genes included in the Immunologic Constant of Rejection (ICR) gene signature to compare between the distinct sarcoma subtypes (22). This 20 gene signature reflects the activation of type 1 T (Th1) cell signalling, expression of CXCR3/CCR5 chemokine ligands, cytotoxicity and counter-activation of immunoregulatory mechanisms and was previously shown to be an independent prognostic factor for metastasis-free survival in soft tissue sarcomas (30). Most chordomas are characterised by a high expression of ICR genes (ICR high) (**figure 1B**), particularly when comparing the ICR score (average of the 20 ICR genes) with samples from other sarcoma types (**figure 1C**). Furthermore, the ICR high immune subtype was associated with improved disease-specific survival in this cohort, albeit only three cases were classified as ICR low (Log rank *P* = 0.0055; **figure 1D**).

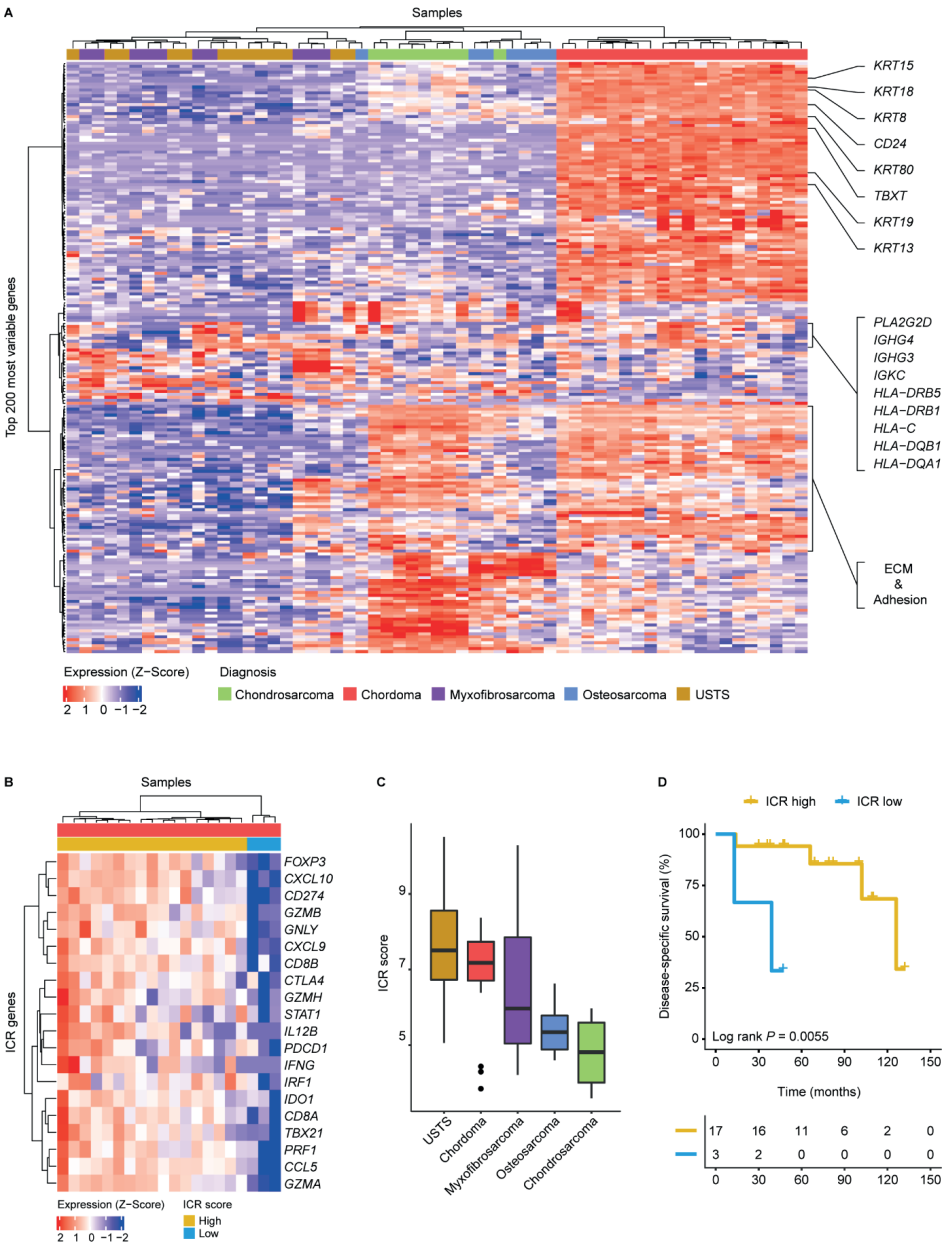

Figure 1 | Chordomas display hallmarks of anti-tumour immunity.

Figure 1 | Chordomas display hallmarks of anti-tumour immunity. A) Heatmap demonstrating the log2 normalised gene expression Z-Score of the top 200 most variably expressed genes in all sarcoma samples (n = 59). Samples are annotated according to their histotype. Genes associated with chordoma samples are highlighted on the right. These genes include chordoma-specific genes such as *TBXT, CD24* and several keratins. In addition, immune-related genes are highlighted, including Human Leukocyte Antigen (*HLA**) and immunoglobulin (*IG**) genes. **B)** Heatmap presenting the Z-Score for the log_2 normalised expression of the 20 ICR signature genes in 20 chordoma samples. Based on the expression Z-Score, the samples are classified into two groups through unsupervised hierarchical clustering: ICR high (n = 17) and ICR low (n = 3). **C)** Boxplots presenting the Immunologic Constant of Rejection (ICR) score per sarcoma subtype in descending order. **D)** Kaplan-Meier curves displaying disease-specific survival for the ICR high and ICR low chordomas. Two-sided log-rank tests were performed for the Kaplan Meier estimates. ECM = extracellular matrix; USTS = undifferentiated soft tissue sarcoma.

T cell infiltration in chordomas correlates with ICR score and separates patients into distinct groups

To confirm and expand our initial observations, we performed imaging mass cytometry to characterise the immune cell contexture of 32 primary tumours. Twenty-nine cell populations were identified including five T cell phenotypes comprising $CD4^+$ T cells, $CD8^+$ T cells, Ki-67^+ T cells, regulatory T cells and (unspecified) T cells including low numbers of $CD57^+$ and gamma delta T cells (**supplemental figure 2**). Since the ICR transcriptional signature is largely reminiscent of T cell-driven immune responses, we investigated the association between T cell infiltration and the ICR score. Indeed, T cell infiltration was more abundant in ICR high chordomas as compared to ICR low samples (**supplemental figure 3A**). Of note, T cells were detected in all chordomas although the levels of infiltration were highly variable, both within and between lesions, ranging from 6.5 to 284.6 cells / mm^2 (median = 51 cells / mm^2) between tumours (**figure 2A, B**). Although the vast majority of T cells was confined to the stromal compartment surrounding the tumour lobules, most tumours also show infiltration of a low number of T cells within the cancer cell compartment. Other commonly observed immune cell populations included various subsets of myeloid cells, such as monocytes, macrophages, dendritic cells, and granulocytes (**supplemental figure 2**).

Next, chordoma samples were clustered according to the extent of infiltration of the different T cell populations leading to the definition of two major groups (high vs. low T cell infiltration; **figure 2C-D**). Of note, infiltration by $CD4^+$ and $CD8^+$ T cells was highly correlated across the cohort (**supplemental figure 3B**). All three chordoma samples previously classified as ICR low clustered in the T cell low group but samples that were previously classified as ICR high were equally distributed between high and low T cell groups (**figure 2C**),

demonstrating the additional value of image-based evaluation of immune cell infiltration in solid tumours. Although it appeared that patients with higher T cell infiltration have an improved disease-specific survival, the observed association was not statistically significant (Log rank *P* = 0.11, **figure 2E**). There was no association between T cell infiltration and recurrence- or metastasis-free survival (**supplemental figure 4A-B**). Moreover, unsupervised clustering of sequential tumours of six patients revealed that the immune contexture of chordomas can change upon disease recurrence or metastasis (**supplemental figure 4C**).

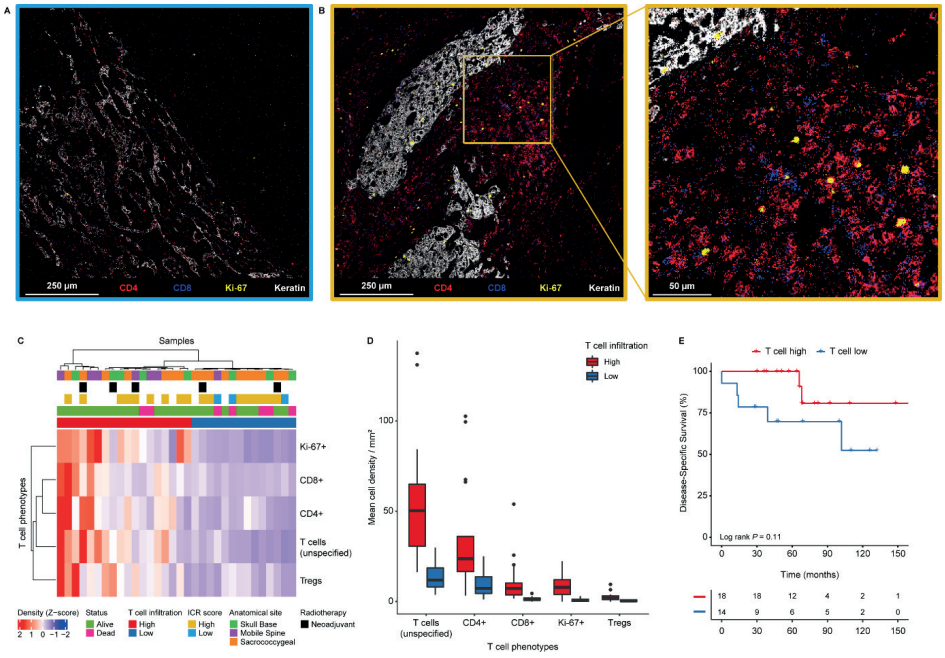

Figure 2 | Chordomas present distinct groups based on T cell infiltration. A-B) Heterogeneity in T cell infiltration in chordomas. The images show T cell-related markers (CD4 = red, CD8 = blue), a proliferation marker (Ki-67 = yellow) and a tumour marker (keratin = white) as detected by imaging mass cytometry. **A)** chordoma with low T cell infiltration (ICR low). **B)** chordoma with high T cell infiltration and a magnified image of the chordoma with high T cell infiltration (ICR high). **C)**, Heatmap showing the mean cell density Z-Score of all T cell phenotypes in all chordoma samples (n = 32), hierarchically clustered into a T cell high (n = 18) and T cell low (n = 14) group. Samples are annotated with their respective ICR score from the transcriptional analysis. In addition, the samples are annotated for their anatomical location, the follow-up status of the patients as well as whether the sample had received neoadjuvant radiotherapy. **D)** Boxplots presenting the mean cell densities per mm² per classified T cell group (T cell high: n = 18; T cell low: n = 14) for the identified T cell phenotypes. **E)** Kaplan-Meier curves interrogating the association between T cell infiltration and disease-specific survival. Two-sided log-rank tests were performed for the Kaplan Meier estimates. ICR = immunologic constant of rejection; Tregs = regulatory T cells.

Antigen-presenting myeloid cells are abundant in T cell high chordomas and co-localise with T cells

Further exploration of the imaging mass cytometry data revealed that high T cell infiltration was accompanied by the presence of dendritic cells (T cell high vs T cell low, $P < 0.001$, Benjamini-Hochberg corrected false discovery rate [FDR] = 0.0052, **figure 3A**). In addition, we found that T cell high chordomas were characterised by increased numbers of immune cell aggregates mainly composed of T cells and myeloid cells ($P < 0.001$, FDR = 0.0052, **figure 3A**). Other phenotypes that were significantly associated with T cell infiltration include CD11c$^+$HLA-DR$^+$ macrophages ($P = 0.014$, FDR = 0.048), CD163$^+$HLA-DR$^+$ macrophages ($P = 0.0079$, FDR = 0.035), granulocytes ($P = 0.0082$, FDR = 0.035), podoplanin$^+$ stromal cells ($P < 0.001$, FDR = 0.0052) and vessels ($P = 0.0088$, FDR = 0.035; **supplemental figure 5A-B**). No specific phenotypes were associated with low T cell infiltration. Instead, this group exhibited a significantly lower density of immune cells ($P < 0.001$) and stromal cells ($P < 0.01$), resulting in a higher relative proportion of tumour cells (**supplemental figure 5C**). HLA class II expression (HLA-DR) was only detected on immune cell populations and never on tumour cells.

A comparative neighbourhood analysis on the imaging mass cytometry data was conducted to reveal distinct interaction patterns between both T cell groups independent of their overall abundance (**figure 3C**). Naturally, most interactions involving T cells were enriched in the T cell high group, where most T cell phenotypes interacted with each other, with the exception of regulatory T cells which were only enriched in the neighbourhood of CD39$^+$ stromal cells (**figure 3C**) The pro-inflammatory nature of the microenvironment of T cell high chordomas was further reinforced by the observed interactions between dendritic cells and CD8$^+$ and Ki-67$^+$ T cells as well as CD38$^+$ plasma B cells and CD4$^+$ and unspecified T cells (**figure 3C**). Most notably, the co-localisation of Ki-67$^+$ T cells with CD4$^+$ T cells and dendritic cells suggests interaction between these anti-tumour immune cells in a coordinated manner. In contrast, the most dominant interactions in the microenvironment of T cell low chordomas involved macrophage and stromal cell subsets including CD163$^+$HLA-DR$^+$ macrophages, stromal cells, vessels and CD39$^+$ vessels (**figure 3C**). These observations suggest that the presence of T cells in T cell high chordomas accompanies a coordinated inflammatory response that also involves antigen-presenting myeloid cells such as dendritic cells, whereas the T cell low chordomas appear to be dominated with myeloid and stromal cell interactions.

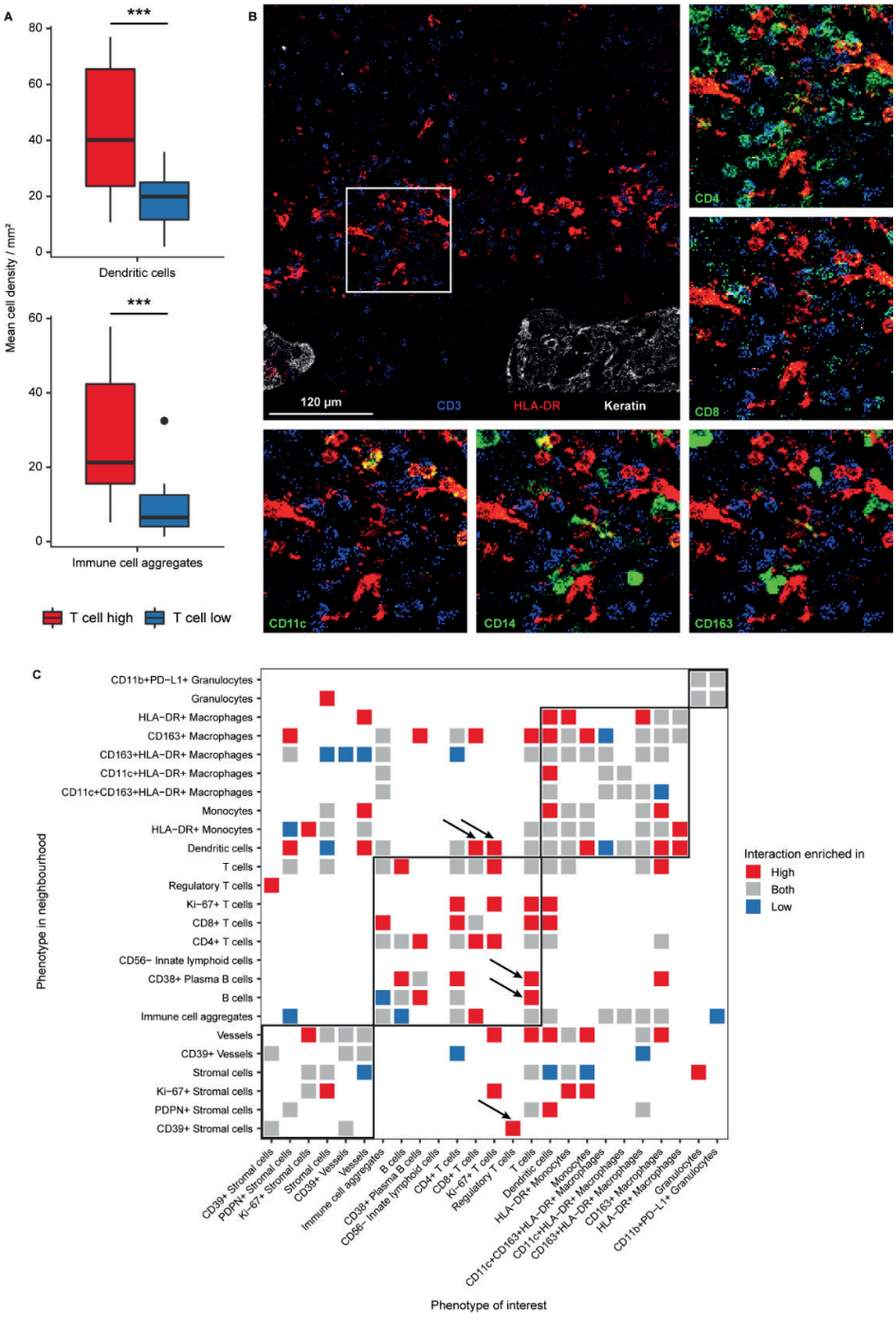

Figure 3 | Pro-inflammatory interactions shape the immune microenvironment of T cell high chordomas.

Figure 3 | Pro-inflammatory interactions shape the immune microenvironment of T cell high chordomas. A) Boxplots comparing cell densities between the T cell high (n = 18) and T cell low groups (n = 14). Dendritic cells ($CD11c^{+/-}HLA\text{-}DR^{+}CD68^{-}$) and immune cell aggregates ($CD45^{+}$ and multiple differentiation markers, e.g. $CD3^{+}CD68^{+}$) are significantly higher in the T cell high group as compared to the T cell low group. Two-sided t-test was performed in R and the P value was adjusted with the Benjamini-Hochberg false discovery rate (FDR). * = P < 0.05; ** = P < 0.01; *** P < 0.001. **B)**, An image generated with imaging mass cytometry displaying co-localisation of dendritic cells (HLA-DR = red) and T cells (CD3 = blue). Tumour cells are only shown in the overview image (top-left image, keratin = white). Other myeloid and T cell-related markers are presented in separate images around the overview image in green (CD4, CD8, CD11c, CD14 and CD163), to show co-localisation of different markers. **C)** Heatmap displaying the spatial interaction analysis results comparing the microenvironment of T cell high with T cell low chordomas. Only significant interactions are visualised and coloured for the subgroup(s) in which they are enriched. Permutation Z scores below 10 were considered not significant and thus removed for visualisation. Interactions of interest are indicated by black arrows. PDPN = podoplanin.

The extent of T cell infiltration in chordomas is independent of clinical parameters

To further explore the relation between the microenvironment of chordomas and the clinical behaviour of the disease, we performed multispectral immunofluorescence on the complete patient cohort (*n* = 76). A T cell-orientated antibody panel was designed to evaluate the expression of CD3, CD8, FoxP3, Ki-67 and pan-cytokeratin. Following cell phenotyping and automated counting, patients were clustered into T cell high and low groups (**figure 4A, B**). Also in this cohort, a positive correlation was observed between $CD4^{+}$ and $CD8^{+}$ T cell infiltration (**supplemental figure 6A**). No significant association was found between T cell infiltration and disease-specific survival (Log-rank *P* = 0.17, **figure 4C**). Further, we have investigated a potential effect of specific T cell phenotypes but not association with survival was found (supplemental table 5). Of note, a higher proportion of KI-67+ cells was found in the $CD8^{+}$ T cell population when compared to $CD4^{+}$ T cells (*P* = 0.006, **supplemental figure 6B**).

Clinical features, such as anatomical location of the tumour or neoadjuvant radiotherapy, were not associated with T cell infiltration, suggesting that the presence of a coordinated immune response is not dependent on neoadjuvant radiation or the tumour's location (**figure 4A**). Further associations between clinical parameters and prognosis were explored through cox proportional hazard models for the disease-specific, recurrence-free and metastasis-free survival, which are all presented in **supplemental table 6**. In short, previously established clinical parameters such as anatomical location of the primary tumour or the surgical resection margin were confirmed as prognostic factors.

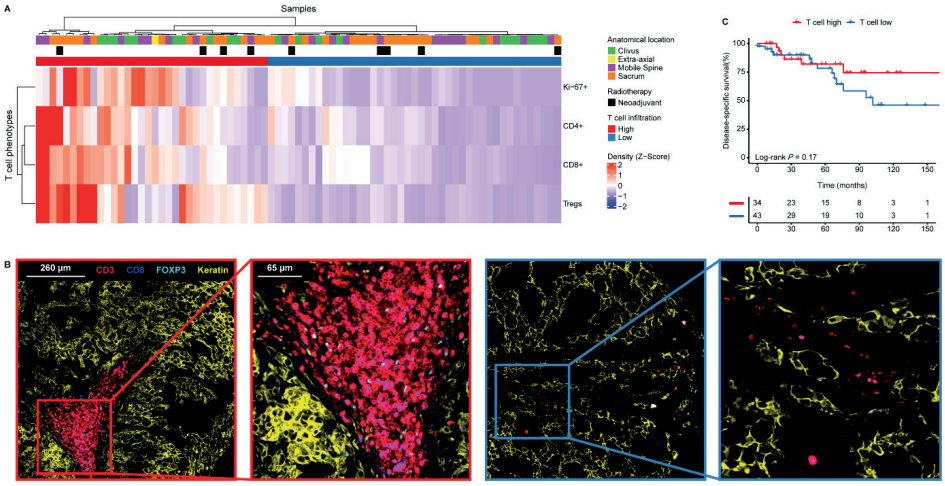

Figure 4 | T cell infiltration is independent from clinical parameters A), Heatmap displaying the mean cell density Z-Score per T cell phenotype as identified with multispectral immunofluorescence in the entire cohort (n = 76). The samples are clustered in an unsupervised manner and thereby marked as T cell high (n = 34) or T cell low (n = 42). The samples are annotated for their respective anatomical location and whether they had received radiotherapy prior. **B)** Images displaying different T cell infiltration patterns as generated by multispectral immunofluorescence. The original and magnified images show T cell-related markers (CD3 = red, CD8 = blue, FOXP3 = cyan) and a tumour marker (keratin = yellow) in two chordomas, each annotated for their respective T cell group (T cell high = red rectangles; T cell low = blue rectangles). **C)** Kaplan-Meier curves of the disease-specific survival comparing the T cell high an T cell low groups of the entire cohort. Two-sided log-rank tests were performed for the Kaplan Meier estimates. Tregs = regulatory T cells.

Figure 5 | Antigen presentation and T cell clonal enrichment are present in chordomas. A) Human Leukocyte Antigen (HLA) class I (HCA2 and HC10) and β-2m expression patterns as validated by immunohistochemistry presenting the distinct expression patterns. From top to bottom, these images display positive expression of HLA class I and thus also β-2m, weak expression of HLA class I and β-2m and defective expression of HLA class I accompanied by weak expression of β-2m. **B)** Stacked bar plots displaying the percentual distribution of the observed HLA class I (both HCA2 and HC10) expression patterns in the chordoma samples in both T cell groups (T cell high: n = 34; T cell low: n = 40) **C-D)** Boxplots displaying the Shannon diversity **C)** and the number of unique clones **D)** of the profiled T cell receptors (TCR) from the immune microenvironment of chordomas (n = 23). Both the Shannon diversity and the number of unique clones are compared between the T cell high (n = 10) and the T cell low (n = 13) groups. Two-sided t-tests were performed to compare the T cell high and the T cell low group. * = P < 0.05; ns = not significant (P > 0.05). **E)** Boxplots presenting the Shannon diversity in relation to the observed HLA class I expression patterns in the subset that underwent TCR profiling (n = 22).

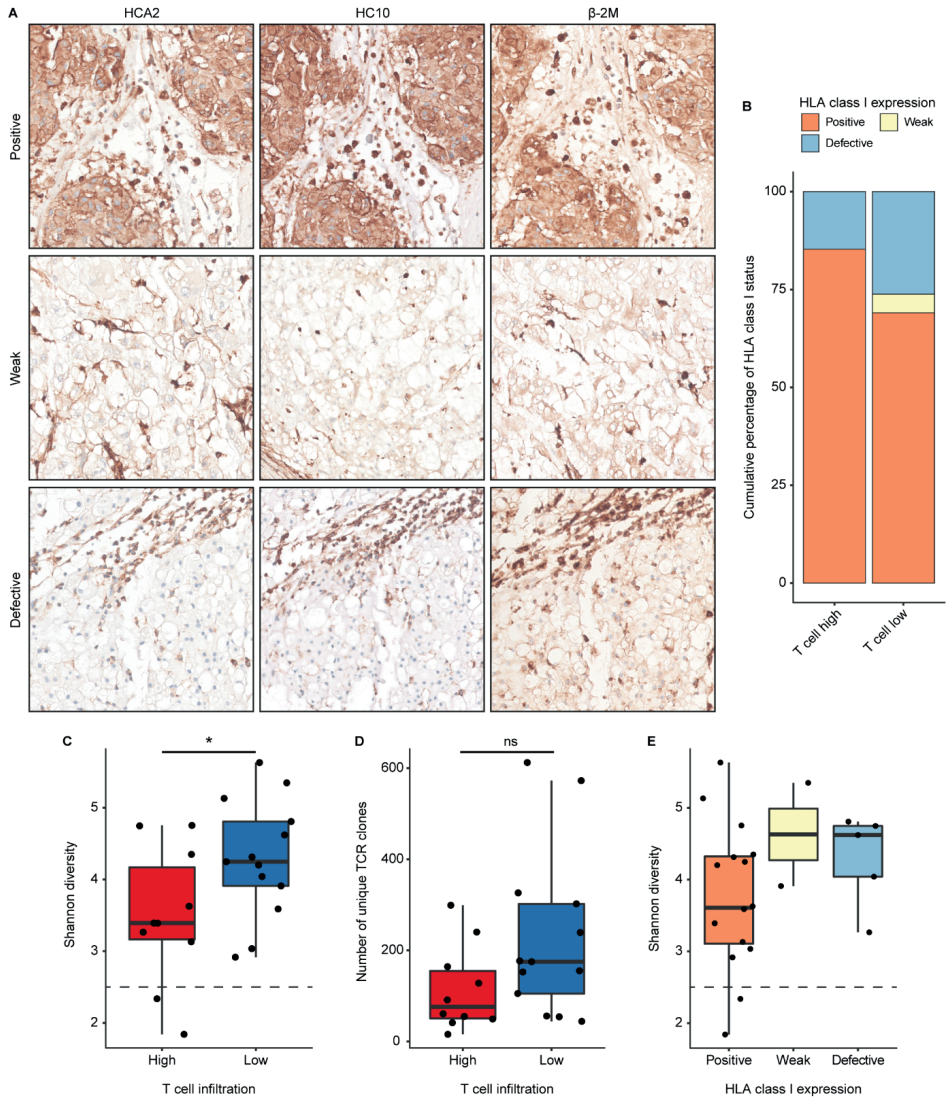

Figure 5 | Antigen presentation and T cell clonal enrichment are present in chordomas.

HLA class I expression is maintained in chordomas, but strong clonal expansion of T cells is rare

Strong immune selective pressure by T cells can lead to immune evasion by tumour cells, most notoriously through loss of HLA class I expression. Since high expression of HLA class I-related genes on RNA level does not preclude the loss of HLA class I expression due to, for instance, mutations in the *B2M* gene, we investigated the prevalence of HLA class I defects by immunodetection (**figure 5A**). In the complete cohort, HLA class I and β-2m membranous expression was observed in the majority of chordomas (73%). However, 22% of chordomas displayed defective HLA class I expression, which was accompanied by either loss or low expression of β-2m. The remaining 5% of the cases showed very weak expression of HLA class I and/or β-2m, which was identified by stronger stromal expression of HLA class I/β-2m but weak expression in the tumour cells. Thus, up to 27% of chordoma samples presented some form of impaired or altered antigen presentation. Interestingly, patients in the T cell low group more often had defective or weak HLA class I expression in comparison to T cell high patients (**figure 5B**). Positivity for HLA class I was relatively more frequent in T cell high patients (**figure 5B**). HLA class I expression was also examined specifically in the context of $CD8^+$ T cell infiltration but no association between HLA class I phenotypes and $CD8^+$ T cell infiltration was found (**supplemental figure 6C**). Intriguingly, we observed intratumoral γδ T cell infiltration in one T cell high chordoma lacking HLA class I expression (**supplemental figure 7A-B**). γδ T cells have recently been proposed as effectors of immunotherapy in HLA class I-defective cancers (31). These results indicate that HLA class I expression and, therefore, antigen presentation is maintained in the majority of chordomas.

Presentation of tumour antigens can lead to the specific enrichment of T cell clones with anti-tumour specificity in the tumour tissues. To investigate the clonality of T cell responses in chordomas, we sequenced the variable region of the *TCRB* locus in 27 chordoma samples from 23 patients. Intriguingly, T cell high chordomas presented a more focused TCR repertoire than T cell low chordomas, which was demonstrated by the lower number of unique clones ($P = 0.068$) and Shannon diversity ($P = 0.047$) in T cell high chordomas compared to T cell low chordomas (**figure 5C-D**). Additionally, tumours displaying a Shannon diversity below 2.5 were only contained within the T cell high group, suggesting the presence of strong clonal expansion in two T cell high chordomas (**figure 5C**). To substantiate the evidence for enriched TCR clonality, the Shannon diversity was compared to the HLA class I expression pattern of these 23 tumours, which revealed that patients with positive HLA class I expression,

presented a more enriched TCR repertoire than patients with either defective or weak HLA class I expression (**figure 5E**).

DISCUSSION

Through a multimodal approach comprising RNA sequencing, imaging mass cytometry, multispectral immunofluorescence and TCR profiling, we studied the immune microenvironment of in total 77 chordoma patients. We found that chordomas present many hallmarks of anti-tumour immunity. We observed the majority of chordomas to have an "immune hot" microenvironment based on their immune-related transcriptomic profile, especially compared to other bone sarcomas (e.g. chondrosarcoma and osteosarcoma). Spatial analysis of immune cell infiltration further defined groups of chordoma patients based on the prevalence of T cell phenotypes. Increased T cell infiltration was associated with an apparently coordinated anti-tumour immune response as indicated by the presence of dendritic cells and other immune cells in immune cell aggregates. In contrast, chordomas with lower T cell infiltration were characterised by a microenvironment dominated by interactions comprising stromal cells and myeloid cells. Neither group was associated with clinical outcome nor with any other clinical parameter.

Recently, several studies have contributed to the improved understanding of the chordoma microenvironment, based on approaches including immunohistochemistry, multispectral immunofluorescence or single cell-RNA sequencing (6, 7, 29, 32, 33). These studies identified myeloid cells and T cells as the most predominant immune cell populations in chordomas (7, 29, 32, 33). Similar to our findings, the majority of these immune cells was confined to the stroma, although both cell types could be found in the tumour nodules (6, 7, 33). Moreover, other lymphoid cells such as NK cells (or innate lymphoid cells) and B cells were considered rare in chordomas (7, 29, 33). Using imaging mass cytometry, we expanded on the previously identified immune cell populations and were able to establish immunologically relevant interactions within the chordoma microenvironment.

Studies focussed on methylation and RNA sequencing have identified groups of patients with either an inflamed or non-inflamed phenotype and associated these groups to clinical outcome, all with varying implications (34-36). For instance, Zuccato *et al.* found through methylation profiling that a group of patients presenting an inflamed phenotype had a worse prognosis than patients without these inflammatory features (35), whereas Huo *et al.*

observed that patients from the non-inflamed group had a worse clinical outcome (34). Furthermore, Baluszcek *et al.* described two similar groups based on methylation and transcriptomic profiling, without finding an association between these groups and survival (36). All these studies, however, either only include skull base chordomas or skull base chordomas combined with spinal chordomas. The variable composition of the cohorts based on institutional referral patterns complicates the identification of common prognostic markers across studies. Here we included tumours from all major anatomical locations as well as different treatment strategies, providing an extensive characterisation of a uniquely large series of chordomas as representative of the general patient population as possible. Presently, the cause of the apparent disconnect between the immune microenvironment and clinical outcomes in chordoma remains uncertain. It is conceivable that the extensive and intricate surgical interventions required for chordoma treatment exert a more significant influence on clinical outcomes than the natural immune response. Future investigations might delve into this by examining the prognostic significance of the immune microenvironment in patients exclusively undergoing radiotherapy. Alternatively, it is plausible that an inadequate cytotoxic T cell response stems from a lack of available CD8+ T cell epitopes due to the low mutation burden of chordomas, offering another potential explanation.

Nevertheless, most studies, including ours, support the separation of distinct groups of chordomas based on the abundance of pro-inflammatory immune cells in their microenvironment. Little is known, however, regarding potential drivers of these different immune contextures. In other tumour types (e.g., melanoma, carcinomas) spontaneous immune responses can often be explained by the mutation burden of a cancer where tumours with high mutation burden more often experience spontaneous anti-tumour immune responses as a consequence of high neoantigen abundance. In contrast, similar to most other sarcomas, the number of somatic, coding mutations in chordomas is generally low and stable between patients making it unlikely that distinct immune responses can be explained by the overall mutation burden of the tumours (13-15, 37). Although we only found evidence for strong clonal expansion in two T cell high chordomas, the TCR repertoire was less diverse in T cell high chordoma than T cell low chordomas, which would support that antigen recognition is a potential driver of immunity in chordomas. Naturally, this raises the question whether there is some specificity for the known chordoma-related transcription factor brachyury (*TBXT*) in these tumours, as it has increasingly been demonstrated that it can be recognised by T cells as

well as that it can be targeted by means of vaccination in chordomas (9, 38). Another possible underlying factor to these distinct groups could be the extent of immunosuppressive mechanisms in the chordoma microenvironment. For instance, we identified abundant CD39 expression on vessels and stromal cells, in the vicinity of immune cells in both T cell high and T cell low chordomas, suggesting that the adenosine pathway might be a potential mediator of immune suppression in chordomas. Although the immunosuppressive functionalities of this pathway have mainly been described in carcinomas (39, 40), expression of CD39 was recently found to associate with increased inflammation in primary tumours as well as with increased T cell densities and PD-1 expression in recurrent undifferentiated soft tissue sarcomas (41). Further research should determine the extent to which the adenosine pathway can modulate immune responses in this disease.

Going forward, it will be crucial to understand how the chordoma microenvironment impacts the outcomes of immunotherapy, in particular immune checkpoint blockade therapy. Intuitively, and as observed in other tumour types, responses should be more likely to occur in patients where spontaneous anti-tumour immune responses are observed. Encouragingly, our data also supports the notion that most chordoma patients may be eligible to immunotherapeutic approaches as: 1) despite differences in the extent of immune infiltration between tumours, the majority of chordomas display enhanced hallmarks of anti-tumour immunity as compared to other sarcoma types and 2) we determined that the majority of chordoma cases retain HLA class I expression and, therefore, antigen presentation. Therefore, other approaches including antigen vaccination or T cell based immunotherapies are, in theory, applicable for chordoma patients and may be particularly important in chordomas that do not present with a conspicuous anti-tumour immune response. We speculate that providing immunotherapy in the neoadjuvant setting (42) to chordoma patients, either with or without radiotherapy, might have a strong impact on the clinical management of these tumours as it might improve surgical outcomes through tumour shrinkage. This could contribute to less extensive and complicated surgical procedures which could either reduce the risk of surgery-related morbidities (e.g. by saving critical nerve structures in the axial skeleton) or possibly facilitate complete surgical resection.

In conclusion, through a multimodal approach we provided evidence that chordomas present multiple hallmarks of anti-tumour immunity. On a transcriptional level, chordomas appear more enriched for inflammatory signalling than other genetically complex sarcomas. Within our chordoma cohort, we identified distinct immune contextures, either defined by a

coordinated, possibly antigen-driven, immune response or a microenvironment dominated by stromal- and myeloid cell interactions. Furthermore, antigen presentation was maintained in the majority of chordomas. Our study provides a rationale for utilising immunotherapeutic strategies to aid in the clinical management of chordomas.

DATA AVAILABILITY STATEMENT

Code & data availability

The RNA sequencing data generated in this study are publicly available on GEO (GSE239531). The imaging mass cytometry data is available on BioImage Archive (S-BIAD830). The RNA sequencing data for the other studied sarcoma subtypes is unpublished and therefore not yet available, with the exception of the osteosarcomas (GSE237033). The used code and processed data are published on our group's GitLab (**https://git.lumc.nl/bstp/papers/multimodal-profiling-of-chordomas)** and GitHub (**https://github.com/demirandalab/multimodal-profiling-of-chordomas**) for reproducibility. All other data are available from the corresponding author on reasonable request.

ETHICS STATEMENT

Patient consent

A waiver of consent was obtained from the medical ethical evaluation committee (protocol number: B17.039 and B21.009).

Ethical approval

All specimens in this study were pseudo anonymised and handled according to the ethical guidelines described in 'Code for Proper Secondary Use of Human Tissue in The Netherlands' of the Dutch Federation of Medical Scientific Societies.

ACKNOWLEDGMENTS

The authors would like to thank the Flow Core Facility and the Information Technology & Digital Innovation department of the Leiden University Medical Center for their service.

REFERENCES

1. WHO Classification of Tumours Editorial Board. Soft Tissue and Bone Tumours. WHO Classification of Tumours. 5 ed. Lyon, France: IARC Publications; 2020.
2. Walcott BP, Nahed BV, Mohyeldin A, Coumans JV, Kahle KT, Ferreira MJ. Chordoma: current concepts, management, and future directions. Lancet Oncol. 2012;13(2):e69-76.
3. Stacchiotti S, Gronchi A, Fossati P, Akiyama T, Alapetite C, Baumann M, et al. Best practices for the management of local-regional recurrent chordoma: a position paper by the Chordoma Global Consensus Group. Ann Oncol. 2017;28(6):1230-42.
4. Smoll NR, Gautschi OP, Radovanovic I, Schaller K, Weber DC. Incidence and relative survival of chordomas: the standardized mortality ratio and the impact of chordomas on a population. Cancer. 2013;119(11):2029-37.
5. Colia V, Stacchiotti S. Medical treatment of advanced chordomas. Eur J Cancer. 2017;83:220-8.
6. Patel SS, Nota SP, Sabbatino F, Nielsen GP, Deshpande V, Wang X, et al. Defective HLA Class I Expression and Patterns of Lymphocyte Infiltration in Chordoma Tumors. Clin Orthop Relat Res. 2021;479(6):1373-82.
7. Dridi M, Krebs-Drouot L, Meyronet D, Dumollard JM, Vassal F, Jouanneau E, et al. The Immune Microenvironment of Chordomas: An Immunohistochemical Analysis. Cancers (Basel). 2021;13(13).
8. Wu X, Lin X, Chen Y, Kong W, Xu J, Yu Z. Response of Metastatic Chordoma to the Immune Checkpoint Inhibitor Pembrolizumab: A Case Report. Front Oncol. 2020;10:565945.
9. Williamson LM, Rive CM, Di Francesco D, Titmuss E, Chun HE, Brown SD, et al. Clinical response to nivolumab in an INI1-deficient pediatric chordoma correlates with immunogenic recognition of brachyury. NPJ Precis Oncol. 2021;5(1):103.
10. Somaiah N, Conley AP, Parra ER, Lin H, Amini B, Solis Soto L, et al. Durvalumab plus tremelimumab in advanced or metastatic soft tissue and bone sarcomas: a single-centre phase 2 trial. Lancet Oncol. 2022;23(9):1156-66.
11. Bishop AJ, Amini B, Lin H, Raza SM, Patel S, Grosshans DR, et al. Immune Checkpoint Inhibitors Have Clinical Activity in Patients With Recurrent Chordoma. J Immunother. 2022;45(8):374-8.
12. Blay JY, Chevret S, Le Cesne A, Brahmi M, Penel N, Cousin S, et al. Pembrolizumab in patients with rare and ultra-rare sarcomas (AcSe Pembrolizumab): analysis of a subgroup from a non-randomised, open-label, phase 2, basket trial. Lancet Oncol. 2023.
13. Tarpey PS, Behjati S, Young MD, Martincorena I, Alexandrov LB, Farndon SJ, et al. The driver landscape of sporadic chordoma. Nature Communications. 2017;8.
14. Bai J, Shi J, Li C, Wang S, Zhang T, Hua X, et al. Whole genome sequencing of skull-base chordoma reveals genomic alterations associated with recurrence and chordoma-specific survival. Nat Commun. 2021;12(1):757.
15. van Oost S, Meijer DM, Kuijjer ML, Bovee J, de Miranda N. Linking Immunity with Genomics in Sarcomas: Is Genomic Complexity an Immunogenic Trigger? Biomedicines. 2021;9(8).

16. D'Angelo SP, Shoushtari AN, Agaram NP, Kuk D, Qin LX, Carvajal RD, et al. Prevalence of tumor-infiltrating lymphocytes and PD-L1 expression in the soft tissue sarcoma microenvironment. Hum Pathol. 2015;46(3):357-65.

17. Chalmers ZR, Connelly CF, Fabrizio D, Gay L, Ali SM, Ennis R, et al. Analysis of 100,000 human cancer genomes reveals the landscape of tumor mutational burden. Genome Med. 2017;9(1):34.

18. Lam SW, Kostine M, de Miranda N, Schoffski P, Lee CJ, Morreau H, et al. Mismatch repair deficiency is rare in bone and soft tissue tumors. Histopathology. 2021.

19. Petitprez F, de Reynies A, Keung EZ, Chen TW, Sun CM, Calderaro J, et al. B cells are associated with survival and immunotherapy response in sarcoma. Nature. 2020;577(7791):556-60.

20. Italiano A, Bessede A, Pulido M, Bompas E, Piperno-Neumann S, Chevreau C, et al. Pembrolizumab in soft-tissue sarcomas with tertiary lymphoid structures: a phase 2 PEMBROSARC trial cohort. Nat Med. 2022;28(6):1199-206.

21. Anders S, Pyl PT, Huber W. HTSeq--a Python framework to work with high-throughput sequencing data. Bioinformatics. 2015;31(2):166-9.

22. Bertucci F, Finetti P, Simeone I, Hendrickx W, Wang E, Marincola FM, et al. The immunologic constant of rejection classification refines the prognostic value of conventional prognostic signatures in breast cancer. Br J Cancer. 2018;119(11):1383-91.

23. Ijsselsteijn ME, van der Breggen R, Sarasqueta AF, Koning F, de Miranda NFCC. A 40-Marker Panel for High Dimensional Characterization of Cancer Immune Microenvironments by Imaging Mass Cytometry. Front Immunol. 2019;10.

24. Somarakis A, Van Unen V, Koning F, Lelieveldt B, Hollt T. ImaCytE: Visual Exploration of Cellular Micro-Environments for Imaging Mass Cytometry Data. IEEE Trans Vis Comput Graph. 2021;27(1):98-110.

25. Ijsselsteijn ME, Brouwer TP, Abdulrahman Z, Reidy E, Ramalheiro A, Heeren AM, et al. Cancer immunophenotyping by seven-colour multispectral imaging without tyramide signal amplification. J Pathol Clin Res. 2019;5(1):3-11.

26. Ijsselsteijn ME, Petitprez F, Lacroix L, Ruano D, van der Breggen R, Julie C, et al. Revisiting immune escape in colorectal cancer in the era of immunotherapy. Br J Cancer. 2019;120(8):815-8.

27. Nelson AC, Pillay N, Henderson S, Presneau N, Tirabosco R, Halai D, et al. An integrated functional genomics approach identifies the regulatory network directed by brachyury (T) in chordoma. J Pathol. 2012;228(3):274-85.

28. Duan W, Zhang B, Li X, Chen W, Jia S, Xin Z, et al. Single-cell transcriptome profiling reveals intra-tumoral heterogeneity in human chordomas. Cancer Immunol Immunother. 2022;71(9):2185-95.

29. Zhang Q, Fei L, Han R, Huang R, Wang Y, Chen H, et al. Single-cell transcriptome reveals cellular hierarchies and guides p-EMT-targeted trial in skull base chordoma. Cell Discov. 2022;8(1):94.

30. Bertucci F, Niziers V, de Nonneville A, Finetti P, Mescam L, Mir O, et al. Immunologic constant of rejection signature is prognostic in soft-tissue sarcoma and refines the CINSARC signature. J Immunother Cancer. 2022;10(1).

31. de Vries NL, van de Haar J, Veninga V, Chalabi M, Ijsselsteijn ME, van der Ploeg M, et al. gammadelta T cells are effectors of immunotherapy in cancers with HLA class I defects. Nature. 2023;613(7945):743-50.

32. Dancsok AR, Gao D, Lee AF, Steigen SE, Blay JY, Thomas DM, et al. Tumor-associated macrophages and macrophage-related immune checkpoint expression in sarcomas. Oncoimmunology. 2020;9(1):1747340.

33. Lopez DC, Robbins YL, Kowalczyk JT, Lassoued W, Gulley JL, Miettinen MM, et al. Multispectral immunofluorescence evaluation of the myeloid, T cell, and natural killer cell tumor immune microenvironment in chordoma may guide immunotherapeutic strategies. Front Oncol. 2022;12:1012058.

34. Huo X, Guo T, Wang K, Yao B, Li D, Li H, et al. Methylation-based reclassification and risk stratification of skull-base chordomas. Front Oncol. 2022;12:960005.

35. Zuccato JA, Patil V, Mansouri S, Liu JC, Nassiri F, Mamatjan Y, et al. DNA methylation-based prognostic subtypes of chordoma tumors in tissue and plasma. Neuro Oncol. 2022;24(3):442-54.

36. Baluszek S, Kober P, Rusetska N, Wagrodzki M, Mandat T, Kunicki J, et al. DNA methylation, combined with RNA sequencing, provide novel insight into molecular classification of chordomas and their microenvironment. Acta Neuropathol Commun. 2023;11(1):113.

37. Bai J, Shi J, Zhang Y, Li C, Xiong Y, Koka H, et al. Gene Expression Profiling Identifies Two Chordoma Subtypes Associated with Distinct Molecular Mechanisms and Clinical Outcomes. Clin Cancer Res. 2023;29(1):261-70.

38. DeMaria PJ, Bilusic M, Park DM, Heery CR, Donahue RN, Madan RA, et al. Randomized, Double-Blind, Placebo-Controlled Phase II Study of Yeast-Brachyury Vaccine (GI-6301) in Combination with Standard-of-Care Radiotherapy in Locally Advanced, Unresectable Chordoma. Oncologist. 2021;26(5):e847-e58.

39. Allard B, Allard D, Buisseret L, Stagg J. The adenosine pathway in immuno-oncology. Nat Rev Clin Oncol. 2020;17(10):611-29.

40. Xia C, Yin S, To KKW, Fu L. CD39/CD73/A2AR pathway and cancer immunotherapy. Mol Cancer. 2023;22(1):44.

41. Lazcano R, Barreto CM, Salazar R, Carapeto F, Traweek RS, Leung CH, et al. The immune landscape of undifferentiated pleomorphic sarcoma. Front Oncol. 2022;12:1008484.

42. Patel SP, Othus M, Chen Y, Wright GP, Jr., Yost KJ, Hyngstrom JR, et al. Neoadjuvant-Adjuvant or Adjuvant-Only Pembrolizumab in Advanced Melanoma. N Engl J Med. 2023;388(9):813-23.

FOOTNOTES

Author contributions

S.v.O. contributed to the conceptualisation, methodology, investigation, data curation, data analysis, visualisation, writing-original draft and writing-review editing. **D.M.M.** contributed to the conceptualisation, investigation, data curation, data analysis and writing-review editing. **M.E.IJ.** contributed to the experiments, data analysis and writing-review editing. **J.R.** contributed to the data analysis and writing-review editing. **B.v.d.A.** contributed to the investigation and writing-review editing. **R.v.d.B.** contributed to the investigation and writing-review editing. **I.H.B.d.B.** contributed to the investigation and writing-review editing. **M.v.d.P.** contributed to the investigation and writing-review editing. **P.M.W.K.** contributed to the investigation and writing-review editing. **S.B.P.** contributed to the resources and writing-review editing. **W.C.P.** contributed to the resources and writing-review editing. **R.J.P.v.d.W.** contributed to the resources and writing-review editing. **N.F.C.C.d.M**. contributed to the conceptualisation, methodology, investigation, supervision, writing-original draft and writing-review editing. **J.V.M.G.B.** contributed to the conceptualisation, methodology, investigation, supervision, writing-original draft and writing-review editing.

Funding

This work was financially supported by the intramural Leiden Center for Computational Oncology strategic fund. N.F.C.C.d.M. is funded by the European Research Council (ERC) under the European Union's Horizon 2020 Research and Innovation Program (grant agreement no. 852832) and by the VIDI ZonMW (project number: 09150172110092).

Competing interests

The authors declare no competing interests.

SUPPLEMENTAL METHODS

Patient samples

These TMAs were holding 2-4 cores of 1.6 mm in diameter per tumour, dependent on the source of the material or the morphology of the tumour (two cores: biopsy; three cores: resection/excision etc; four cores: heterogeneous morphology, or separate areas of dedifferentiation). As controls and for orientation purposes, each TMA contained three cores tonsil and three cores placenta, either decalcified with EDTA or formic acid or non-decalcified.

Gene expression analysis

Normalisation and exploratory analysis of the RNA sequencing data was performed in R (v.4.0.2) by using DESeq2 (v. 1.30.1). BiomaRt (R, v.2.46.3) was used to translate the ensemble IDs to known protein coding genes. The most variably expressed genes were determined by calculating the variance per gene across all samples. The immunologic constant of rejection (ICR) gene signature was used to describe the activity state immune microenvironment and to identify distinct immune-related clusters (Th1-related markers: *IFNG*, *STAT1*, *IL12B*, *IRF1*, *TBX21*; CD8+ T cells: *CD8A*, *CD8B*; Immune effector molecules: *GZMA*, *GZMB*, *GZMH*, *PRF1*, *GNLY*; Chemokine ligands: *CXCL9*, *CXCL10*, *CCL5*; Immune suppressive molecules: *IDO1*, *PDCD1*, *CD274*, *CTLA4*, *FOXP3*) (1). The mean of the log2 normalised expression of these 20 genes was used to attribute an ICR "score" to each sample for comparison between the sarcoma subtypes, which was visualised with ggplot2 (R, v.3.3.6). For both the heatmaps in **figure 1**, a Z-Score was calculated per gene to visualise the transcriptional profile of the samples by using the Ward variance method with ComplexHeatmap (R, v.2.11.1). Differential gene expression analysis was performed with DESeq2 comparing chordomas to all other sarcomas. Genes were considered differentially expressed when the log2 fold change was above 2 and the adjusted *P* value was below 0.01. Immune-related genes were selected for visualisation in the enhanced volcano plot and additional boxplots. For visualisation purposes, the axes of the enhanced volcano plot were manually adjusted as follows: log2 fold change (x-axis) was set between -10 and 10, and the -log10 adjusted *P* (y-axis) was set to a maximum of 100.

Imaging mass cytometry analysis

To correct for variability in signal-to-noise ratios between FFPE sections, the signal intensity of the generated images was normalised at pixel levels by using Matlab (v.R2021a), after which the images were binarised using semi-

automated background removal in Ilastik (v.1.3.3) as described previously (2). Probability masks were generated in Ilastik by using a multicoloured image including the DNA channel, CD45 channel, Keratin channel and Vimentin channel to annotate nucleus, cytoplasm and background. Probability masks were loaded into CellProfiler (v.2.2.0) and used for creating cell segmentation masks. Next, the segmentation masks and binarised images were loaded into ImaCyte (3) to generate single cell-FCS files containing relative frequency of positive pixels for each marker, which were then used for phenotyping in CytoSplore (v.2.3.1) by sequentially utilizing Hierarchical Stochastic Neighbour Embedding (H-SNE) and t-distributed Stochastic Neighbour Embedding (t-SNE). Identified cell phenotypes were loaded into ImaCyte together with the segmentation masks and binarised images, which allows the mapping of the phenotypes back onto the images. Phenotypes per image were extracted to calculate the mean cell density per mm^2 for every sample (one image = one mm^2). An overview of the lineage markers used for phenotype identification is listed in **supplemental table 2**. Patients were clustered into two groups based on the Z-Score normalised mean cell densities per mm^2 of all five identified T cell phenotypes by using the Ward variance method with ComplexHeatmap. Ggplot2 was used to visualise the mean cell densities and to compare them between both T cell groups. For statistical testing, a two-sided student's t-test was performed followed by a Benjamini-Hochberg FDR correction. In addition, an overview heatmap containing all identified phenotypes in the microenvironment of chordomas was visualised with ComplexHeatmap.

Spatial interaction analysis

After phenotype calling, a spatial interaction analysis was performed with ImaCyte for all imaged samples, comparing T cell low with T cell high chordomas. ImaCyte utilises a 1000-iteration permutation test which calculates a Z-Score for the interaction between adjacent cells. However, permutation testing does not adjust for overabundant cell types, such as tumour cells, and is therefore not able to identify meaningful interactions for tumour cells. Because of the range of the calculated Z-Scores, interactions with a Z-Score below 10 were considered not significant and therefore removed for visualisation only. If an interaction Z-Score was higher than 10 in one group and lower than 10 in the other group, this interaction was considered significant for one group. When both Z-Scores were higher than 10, this interaction would be considered significant in both groups. A comparative interaction heatmap between all phenotypes excluding tumour cells was visualised with ggplot2.

Multispectral immunofluorescent imaging of T cells

All TMAs were imaged at 20x, after which the images were processed with inForm (v.2.4), which comprises background removal for each antibody by normalisation of the spectra, and analysed with QuPath (v.0.3.1). Object classification was performed by using the following classes: $CD3^+FOXP3^+$ = Regulatory T cells, $CD3^+CD8^+$ = $CD8^+$ T cells, $CD3^+$ = $CD4^+$ T cells, $CD3^+Ki\text{-}67^+$ = Proliferating T cells, $CD3^-$ = Rest. Counts per image (one image = 1 mm x 1.3 mm) were normalised per patient to counts per mm^2 tissue. Patients were divided into a T cell high and low cluster based on the unsupervised clustering of the Z-scores of all T cell phenotypes.

Survival analysis

For all chordoma patients, Kaplan-Meier curves for the disease-specific survival and recurrence-free survival were generated with the survminer and survival packages (R, v.0.4.9 and v.3.1-12 respectively). The disease-specific survival was considered the survival of a patient until death due to the disease, whereas the recurrence-free survival was considered the time until a patient was diagnosed with a recurrence, thereby excluding patients who did not receive surgery. Since the cohort included many censored cases, the log-rank *P* value was used to estimate the significance of the associations. Known prognostic factors such as the anatomical tumour location excluding the only extra-axial patient, age and type of treatment, surgical margin excluding patients who did not receive surgery and disease recurrence were investigated for their prognostic value, as well as the newly identified T cell infiltration groups. Univariate and multivariate analyses were performed in R according to the cox proportional hazard model. Only clinical parameters that were found significant in the univariate analysis were taken along in the multivariate analysis.

TCR β-chain sequencing

The number of clones and the Shannon diversity, a measure for clonal enrichment, were calculated in R by using productive counts only, meaning that a clone needed at least 10 plus and 10 minus counts. Because recurrences showed similar levels of TCR diversity as their respective primary tumour, we used the TCR repertoire of recurrences for three patients for which there was no frozen material of primary tumours available. Finally, the data was visualised in R using ggplot2.

SUPPLEMENTARY FIGURES

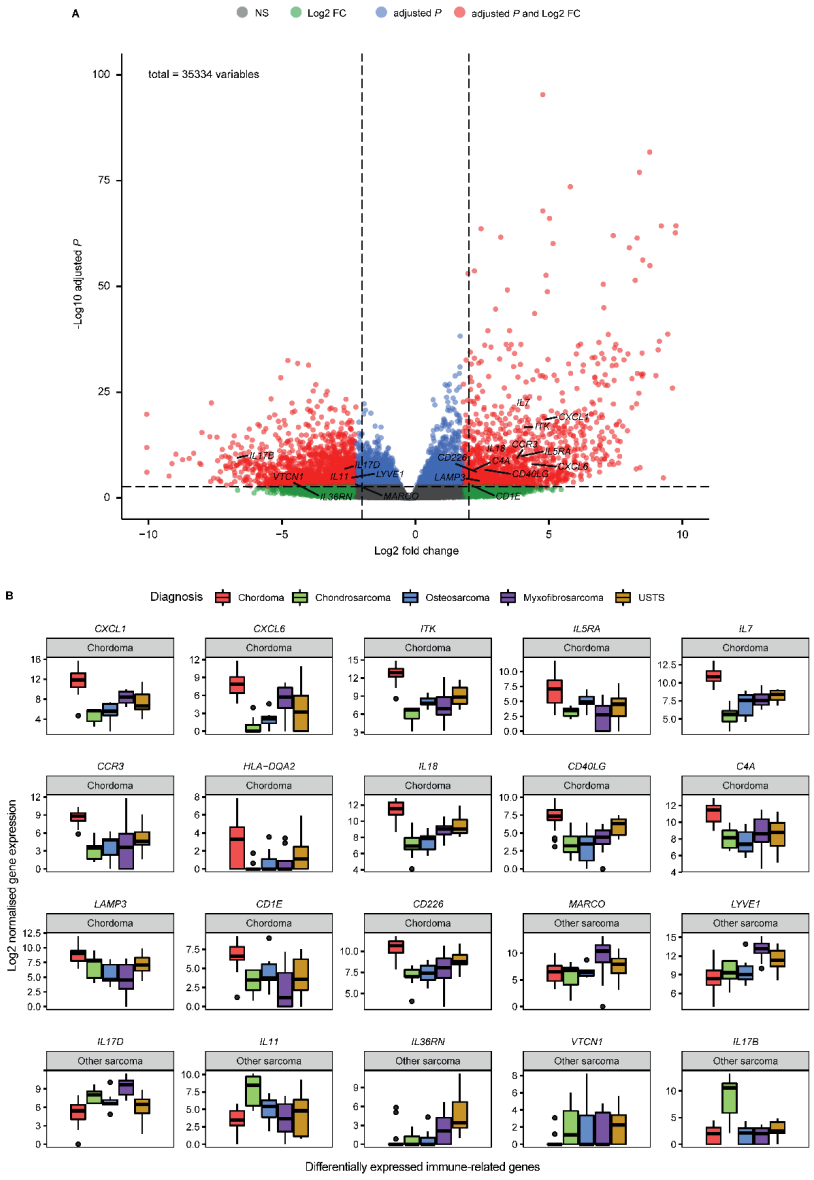

Supplemental figure 1 | Chordomas are enriched for immune-related gene signaling.

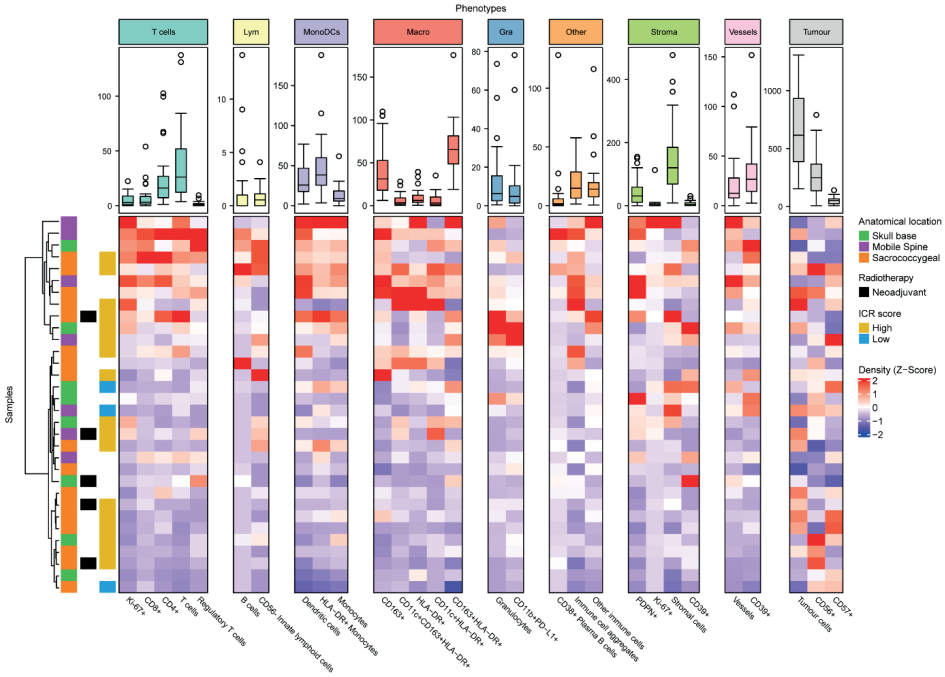

Supplemental figure 2 | Overview of the chordoma microenvironment. Overview heatmap of the mean cell density Z-Score of 29 identified cell phenotypes in all chordoma samples (n = 32). The samples that were used for transcriptome sequencing are annotated according to their ICR score. Samples are hierarchically clustered and annotated for their anatomical location and whether they had received neoadjuvant radiotherapy. Boxplots are presented per phenotype to display the general mean cell densities per mm^2 for each phenotype. ICR = immunologic constant of rejection; Lym = lymphoid; MonoDCs = monocytes and dendritic cells; Macro = macrophages; Gra = granulocytes; PDPN = podoplanin.

Supplemental figure 1 | Chordomas are enriched for immune-related gene signaling. **A)** Enhanced volcano plot presenting the differential gene expression analysis between chordomas (n = 20) and all other studied sarcomas (n = 39. Genes with a log_2 fold change above 2 and an adjusted P value below 0.01 were considered significantly differentially expressed. Immune-related genes were labelled for visualisation. **B)** Boxplots displaying the log_2 normalised expression of the differentially expressed immune related genes. The boxplots are ordered in descending order for the log_2 fold change and annotated for the respective group in which they are significanly enriched (chordoma vs other sarcoma). The boxplots are coloured for their respective histotype. NS = not significant; FC = fold change; USTS = undifferentiated soft tissue sarcoma.

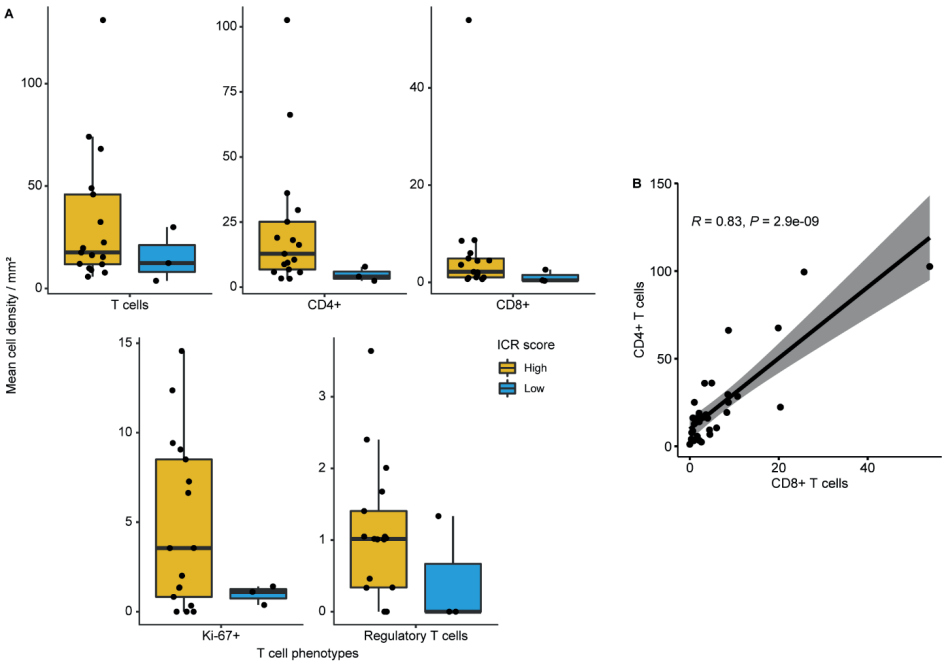

Supplemental figure 3 | ICR high chordomas are enriched with T cell phenotypes. A) Boxplots representing the different levels of infiltration of the identified T cell populations between ICR-high (n = 17) and ICR-low (n = 3) chordomas. No statistical tests were performed due to the small sample size. ICR = immunologic constant of rejection. **B)** Correlation plot presenting the Pearson correlation between $CD4^+$ T cell and $CD8^+$ T cell infiltration based on the imaging mass cytometry data.

Supplemental figure 4 | The immune contexture of chordomas varies over time. A-B) Kaplan-Meier curve indicating the association between T cell infiltration and recurrence-free survival **(A)** as well as metastasis-free survival **(B)**. Two-sided log-rank tests were performed for the Kaplan Meier estimates. **C)** Heatmap presenting the unsupervised clustering of untreated primary tumours (n = 6) and their respective treated primary tumour (n = 1), recurrences (n = 9) and metastases (n = 1). The heatmap displays the mean cell density Z-Score of the identified cell phenotypes, excluding tumour cells. The samples are annotated for patient ID, type of sample, anatomical location, whether the tumour was treated with neoadjuvant radiotherapy and T cell group of the primary tumour. PDPN = podoplanin. ▶

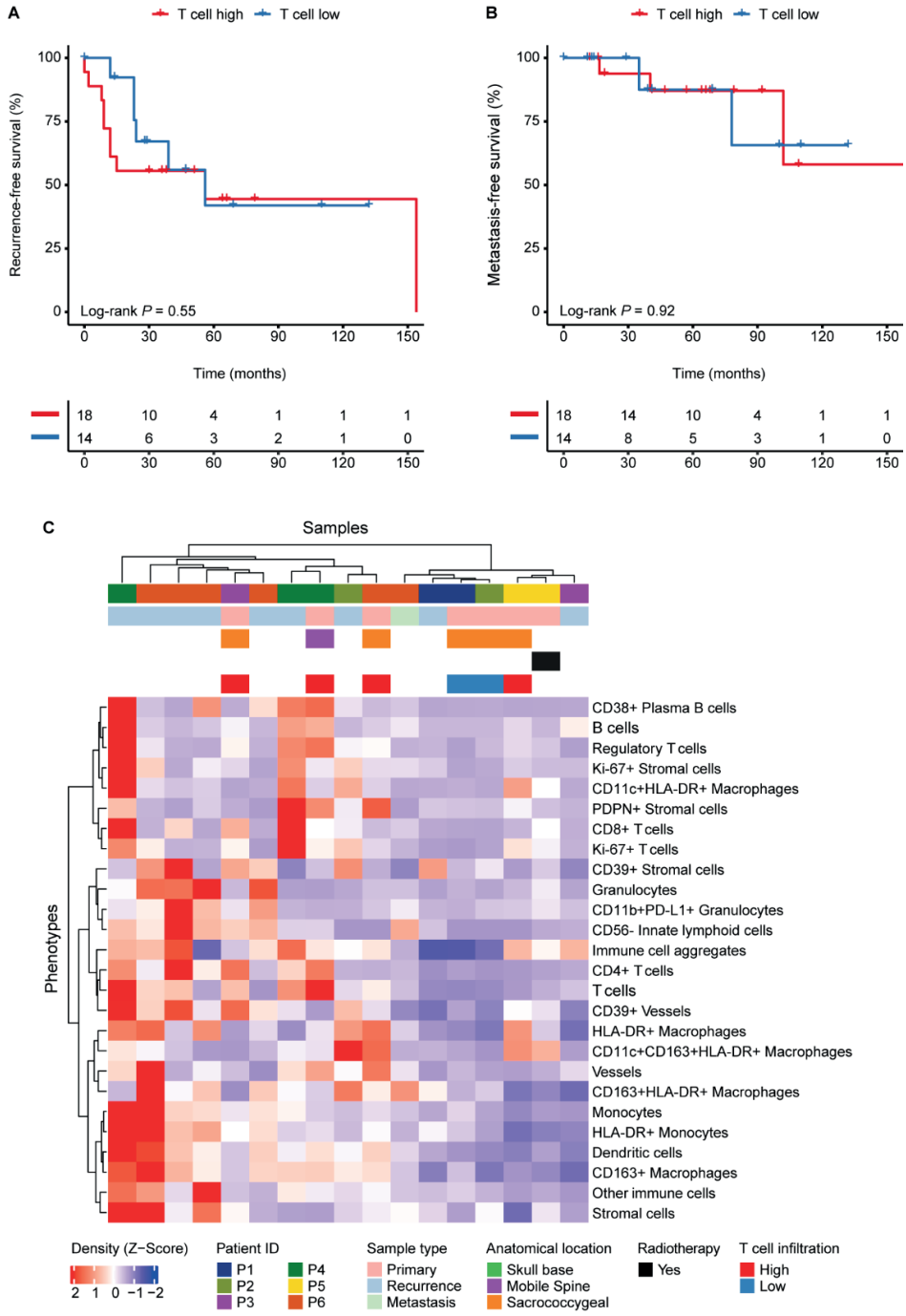

Supplemental figure 4 | The immune contexture of chordomas varies over time.

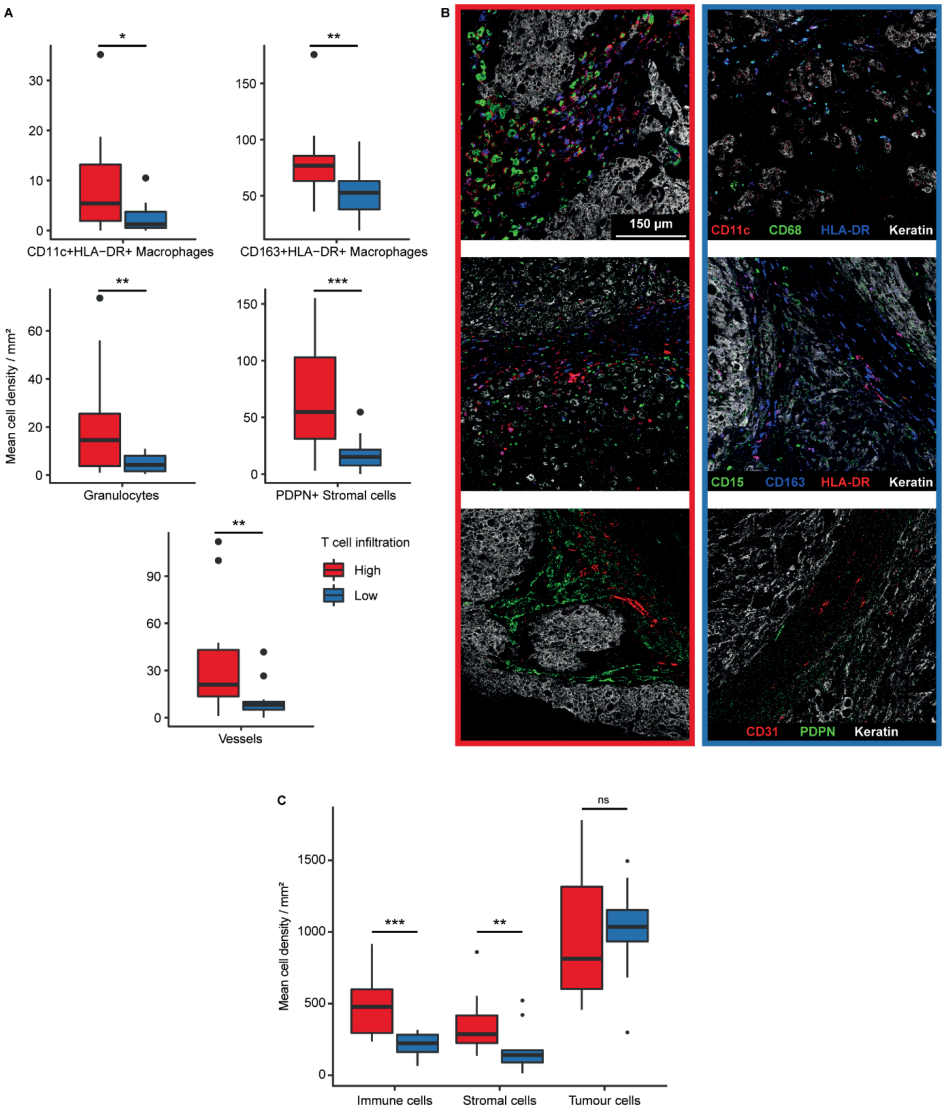

Supplemental figure 5 | Comparative overview of the chordoma immune microenvironment.

Supplemental figure 5 | Comparative overview of the chordoma immune microenvironment. A) Boxplots with the significantly different phenotypes between the T cell high and T cell low groups. Two-sided t-test was performed in R and the P value was adjusted with the Benjamini-Hochberg false discovery rate (FDR). All presented phenotypes were significantly different between the T cell high an T cell low group. * = P < 0.05; ** = P < 0.01; *** P < 0.001. **B)** Representative images generated with imaging mass cytometry displaying the differentially abundant cell phenotypes in both T cell low and T cell high samples. Images are grouped per row for the displayed cell markers and outlined with their respective T cell group (T cell high = red rectangle & left, T cell low = blue rectangle & right). The top row presents $CD11c^+$ macrophages (CD11c = red, CD68 = green, HLA-DR = blue, keratin = white), the middle row displays granulocytes and $CD163^+HLA\text{-}DR^+$ macrophages (CD15 = green, CD163 = blue, HLA-DR = red, keratin = white) and the bottom row shows vessels and $podoplanin^+$ stromal cells (CD31 = red, PDPN = green, keratin = white). **C)** Boxplots presenting the cumulative mean cell density per mm^2 of all immune cells, stromal cells and tumour cells in both T cell high and T cell low groups. Two-sided t-test was performed in R. ** = P < 0.01, *** = P < 0.001. PDPN = podoplanin.

◀

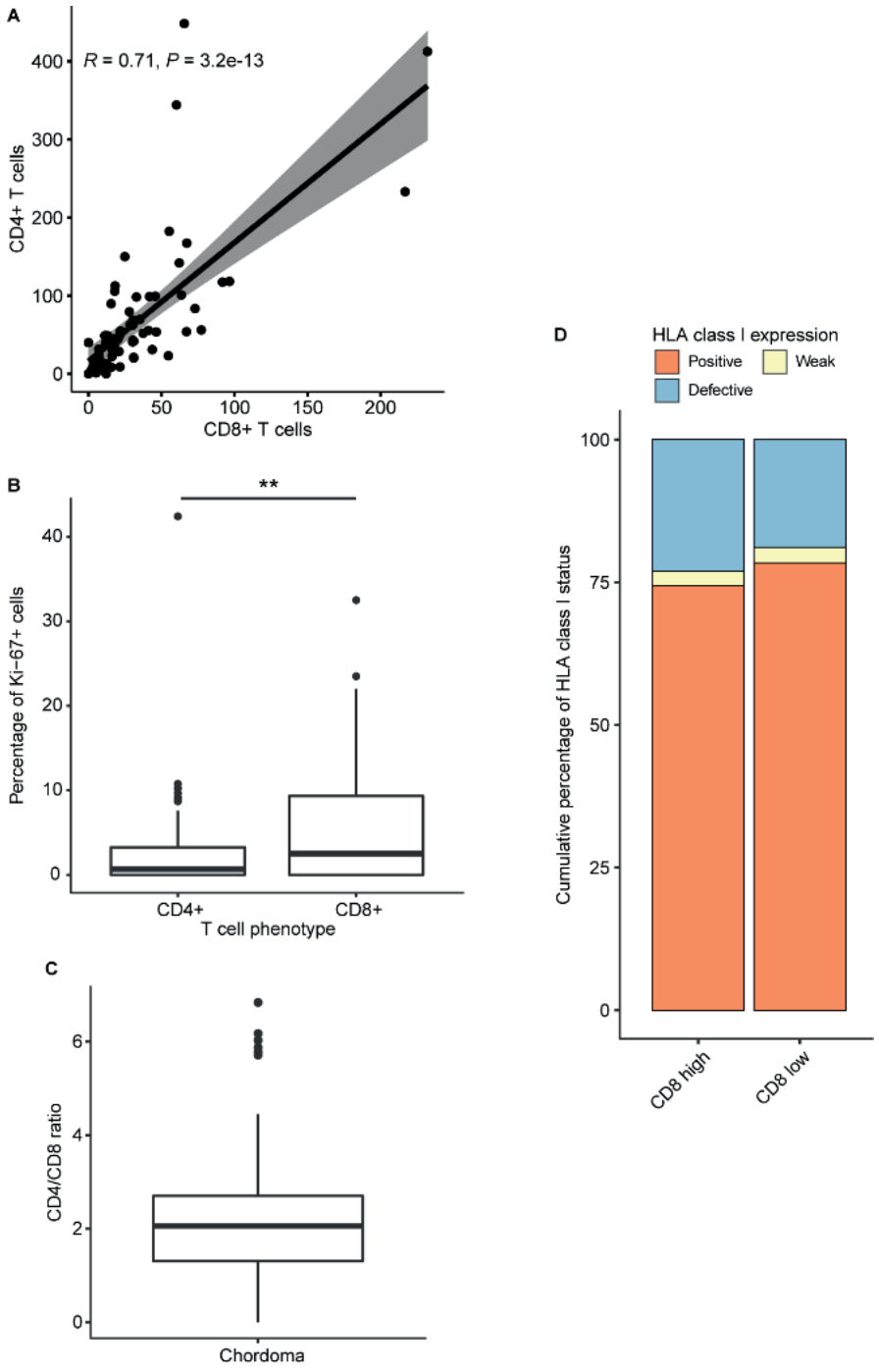

Supplemental figure 6 | CD4⁺ T cell infiltration and HLA class I expression in association with CD8⁺ T cell infiltration.

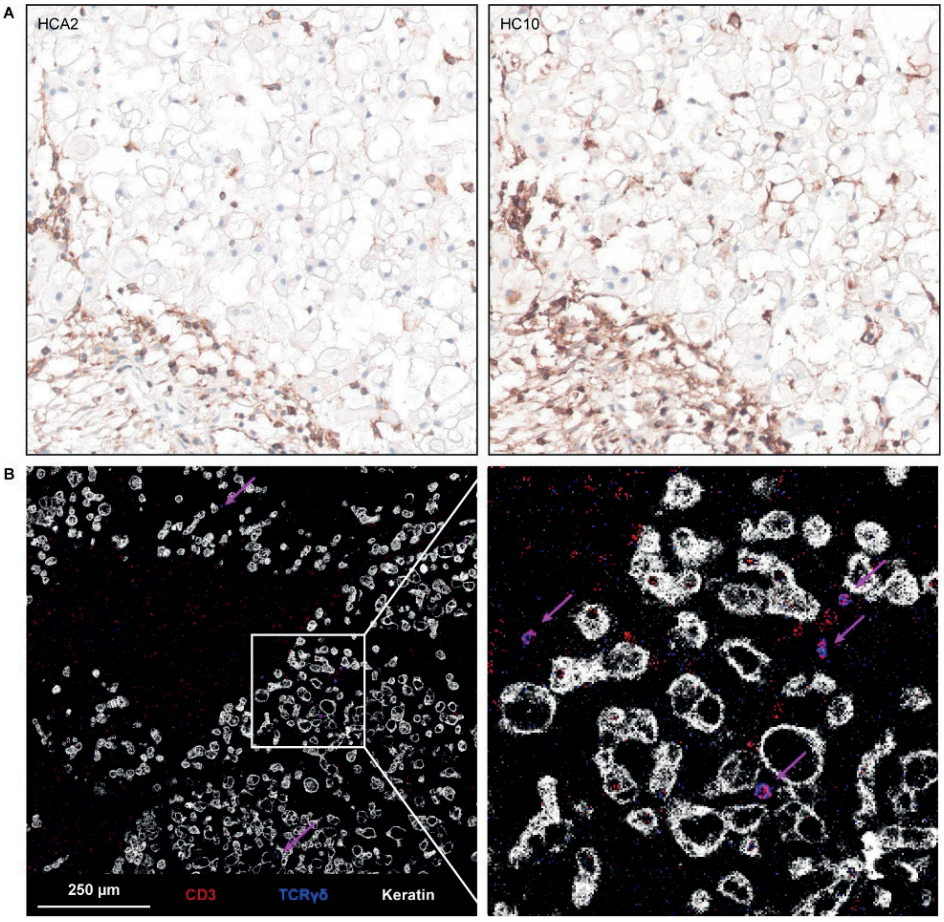

Supplemental figure 7 | γδ T cell infiltration in relation to HLA class I expression. A) Example images of Human Leukocyte Antigen (HLA) class I (HCA2 and HC10) expression in a T cell high chordoma as validated by immunohistochemistry. **B)** An example image and a corresponding magnification of the same tissue core as displayed in **(A)** as generated by imaging mass cytometry. The images present intratumoral γδ T cell infiltration as indicated by the magenta arrows (CD3 = red, TCRγδ = blue, keratin = white). TCR = T cell receptor.

Supplemental figure 6 | $CD4^+$ T cell infiltration and HLA class I expression in association with $CD8^+$ T cell infiltration. A) Correlation plot presenting the Pearson correlation between $CD4^+$ T cell and $CD8^+$ T cell infiltration based on the immunofluorescence data. **B)** Boxplots displaying the percentage of Ki-67+ cells for $CD4^+$ and $CD8^+$ T cells. A two-sided t-test was performed to compare Ki-67^+CD4^+ T cells with Ki-67^+CD8^+ T cells. ** = $P < 0.01$. **C)** Boxplot presenting the CD4/CD8 ratio in chordomas **D)** Stacked bar plots displaying the percentual distribution of the observed HLA class I (both HCA2 and HC10) expression patterns in the chordoma samples divided into $CD8^+$ T cell high and low with the median cell density as cut-off. ($CD8^+$ high: n = 37; $CD8^+$ low: n = 37).Supplemental table 1. Imaging mass cytometry marker panel. Ab = antibody, ON = overnight, PDPN = podoplanin.

Supplemental table 1. Imaging mass cytometry marker panel. Ab = antibody, ON = overnight, PDPN = podoplanin.

	Target	Clone	Metal	Incubation time	Temp	Dilution (x)
Lymphoid	CD103	EPR4166(2)	168 Er	5h	RT	50
	CD20	H1	142 Nd	Overnight	4C	100
	CD3	EP449E	153 Eu	Overnight	4C	50
	CD38	EPR4106	169 Tm	Overnight	4C	100
	CD4 + 2nd AB	EPR6855	145 Nd	Indirect ON	4C	100
	CD7	EPR4242	174 Yb	5h	RT	100
	CD8a	D8A8Y	146 Nd	5h	RT	50
	FOXP3	D608R	159 Tb	Overnight	4C	50
	TCRγδ + 2nd Ab	H41	148 Nd	Indirect ON	4C	50
Myeloid	CD11b	D6X1N	144 Nd	5h	RT	100
	CD11c	EP1347Y	176 Yb	5h	RT	100
	CD14	D7A2T	163 Dy	5h	RT	100
	CD15	MC480	171 Yb	Overnight	4C	100
	CD163	D6U1J	173 Yb	5h	RT	50
	CD204	J5HTR3	164 Dy	5h	RT	50
	CD68	D4B9C	143 Nd	Overnight	4C	100
	HLA-DR	TAL 1B5	141 Pr	5h	RT	100
Stroma	CD31	89C2	147 Sm	Overnight	4C	100
	CD39	EPR20627	157 Gd	5h	RT	100
	CD45	D9M8I	149 Sm	Overnight	4C	50
	CD45RO	UCHL1	165 Ho	Overnight	4C	100
	D2-40 (PDPN)	D2-40	166 Er	Overnight	4C	100
	TGF-β	TB21	115 In	5h	RT	100
	Vimentin	D21H3	194 Pt	Overnight	4C	50
Activation	Cleaved Caspase	5A1E	172 Yb	5h	RT	100
	Granzyme B	D6E9W	150 Nd	5h	RT	100
	ICOS	D1K2T(TM)	161 Dy	5h	RT	50
	IDO	D5J4E(TM)	162 Dy	Overnight	4C	100
	Ki-67	8D5	152 Sm	Overnight	4C	100
	LAG-3	D2G40(TM)	155 Gd	5h	RT	50
	PD-1	D4W2J	160 Gd	5h	RT	50
	PD-L1	E1L3N(R)	156 Gd	Overnight	4C	50
	Tbet	4B10	170 Er	5h	RT	50
	TIM-3	D5D5R(TM)	154 Sm	5h	RT	100
	VISTA	D1L2G(TM)	158 Gd	5h	RT	100

Supplemental table 1. *Continued*

	Target	Clone	Metal	Incubation time	Temp	Dilution (x)
Tumour	CD56	E7X9M	167 Er	5h	RT	100
	CD57	HNK-1 / Leu-7	151 Eu	Overnight	4C	100
	Keratin	C11 and AE1/AE3	198 Pt	Overnight	4C	50
	P16ink4a	D3W8G	175 Lu	Overnight	4C	100
	β-Catenin	D10A8	89 Y	Overnight	4C	100
DNA	Histone H3	D1H2	209 Bi	Overnight	4C	50

Supplemental table 2. Cell type lineage markers imaging mass cytometry. Colours are indicating cell types according to overview heatmap in **supplemental figure 2**. Lineage markers are describing the used markers for cell type identification as used in this study. Lin = lineage markers e.g. CD14 and CD68.

Cell type	Lineage markers
T cells	CD3+
B cells	CD20+
Innate lymphoid cells	CD3-CD7+
Dendritic cells	CD11c+CD68- | Lin-HLA-DR+
Monocytes	CD11c-CD14+CD68-
Immune cells	CD45+
Plasma B cells	CD38+
Macrophages	CD68+
Granulocytes	CD15+
Stromal cells	Vimentin+CD45-
Vessels	CD31+
Tumour cells	Keratin+

Supplemental table 3. Top 200 most variably expressed genes across sarcoma subtypes. Known chordoma-related genes are annotated in **bold** (4-6). Genes are ordered following the heatmap presented in **figure 1A**.

Gene ID	Cluster	Gene ID	Cluster
ENSG00000254626	1	***SHH***	1
HPCAL4	1	*IQCM*	1
CHST4	1	***KRT19***	1
SLC4A11	1	*ENSG00000232110*	1
PKP2	1	***HHLA2***	1
KRT15	1	***RAB3B***	1
NCMAP	1	***KRT13***	1
SALL3	1	*C3orf49*	1
KRT18	1	*CHRM2*	1
KRT8	1	***AKR1B10***	1
C1orf116	1	*LCN1*	1
MTMR7	1	*NPFFR2*	1
ANXA8	1	*GABRA2*	1
ANXA8L1	1	*GPM6A*	1
CD24	1	***NOL4***	1
LGR6	1	*LINC01293*	1
SCUBE1	1	*LINC01291*	1
RIPK4	1	*ALG1L7P*	1
KRT80	1	*ENSG00000290079*	1
CA3	1	*ENSG00000231918*	1
TRIM67	1	***SCEL***	1
AVPR1B	1	*ASTN1*	1
TBXT	1	***ADAMTS19***	1
LNCDAT	1	*LMX1A*	1
PPIAP46	1	*USH2A*	1
ENSG00000285933	1	*LINC00525*	1
GPR101	1	*RASEF*	1
ENSG00000285562	1	*TMPRSS3*	1
MRGPRX3	1	*DLGAP1−AS5*	1
LINC02065	1	*IP6K3*	1
PRSS51	1	*TMPRSS4*	1
ARHGAP40	1	***FAM135B***	1
KCNH6	1	***GDA***	1
ENSG00000280285	1	*LINC02351*	1
SLC15A5	1	*RORC*	1

Supplemental table 3. *Continued*

Gene ID	Cluster
CFAP46	1
POF1B	1
AP3B2	1
NPTX1	1
FAM153B	1
DNAH9	1
CACNA1I	1
MAN1A2P1	1
CNTN3	1
DPP6	1
COL4A6	1
XIRP2	2
ACTA1	2
MYH1	2
MYH2	2
MYH7	2
MYBPC1	2
MYL1	2
PLA2G2D	3
IGHG4	3
IGHG3	3
IGKC	3
HLA−DRB5	3
HLA−DRB1	3
HLA−C	3
HLA−DQB1	3
HLA−DQA1	3
CADM3	4
ADH1B	4
CYP4B1	4
CHRDL1	4
PRG4	4
PI16	4
THBS4	4
RSPO2	4
PLA2G2A	4
GFRA1	4
FEZF1−AS1	4
PAX3	4
EPHA6	4
GSTM1	4
ENSG00000277693	4
DKK1	4
LINC02154	4
XIST	4
PSPHP1	4
MYH14	5
HAPLN1	5
ACAN	5
COL11A1	5
S100A1	5
ITIH6	5
COL2A1	5
COL9A3	5
RFLNA	5
SOX9	5
POU3F3	5
PANTR1	5
FBN3	5
PRSS16	5
CDH19	5
PMP2	5
PCSK2	5
SDR16C5	5
DSP	5
CHST9	5
CNNM1	5
UNC80	5
PCLO	5
SORCS3	5
PWRN1	5
CRTAC1	5
COMP	5
CILP2	5
NGEF	5
KRT16	5

Supplemental table 3. *Continued*

Gene ID	Cluster
SFRP1	5
CXCL14	5
GDF10	5
SCRG1	5
PRELP	5
SEMA3E	5
GABRA1	5
CDH10	5
LGR5	5
SAA1	5
LRRN2	5
SUSD5	5
ECRG4	5
EGF	5
DSC3	5
MMP3	5
DNER	5
EMILIN3	5
ANGPTL7	5
SCN7A	5
MMP13	6
IBSP	6
DMP1	6
MEPE	6
IFITM5	6
PANX3	6
SP7	6
BMP3	6
IGF2BP1	7
FGFBP2	7
COL9A1	7
COL11A2	7
WIF1	7
CHAD	7
CLEC3A	7
COL10A1	7
EPYC	7
MATN3	7
SCUBE3	7

Gene ID	Cluster
CA9	7
MAGEL2	7
KIF1A	7
SLC38A3	7
SHISA9	7
MATN4	7
CNMD	7
PENK	7
DLK1	7
IGF2	7
CAPN6	7
NRK	7
MKX	7
PTPRZ1	7
SLITRK6	7

Supplemental table 4. Top differentially expressed genes comparing chordomas with other sarcomas. Contains the top results from the differential gene expression analysis with DESeq2. Due to the large number of DEGs (>3500), the original table is available as online supplement. Genes with a log2 fold change > 2 and an adjusted P < 0.01 were considered significantly differentially expressed. Known immune-related genes are annotated in the column "hgnc_symbol" with a yellow-filled cell. lfcSE = log fold change standard error; FDR = false discovery rate.

ensembl_gene_id	baseMean	log2FoldChange	lfcSE	pvalue	FDR	hgnc_symbol
ENSG00000179826	7965.996	13.652	0.525	3.56E-149	1.26E-144	*MRGPRX3*
ENSG00000163632	1630.580	13.624	0.600	3.64E-114	4.29E-110	*C3orf49*
ENSG00000260266	11851.775	11.826	0.758	8.39E-55	9.56E-52	*PPIAP46*
ENSG00000164690	1787.949	11.419	0.556	1.24E-93	6.25E-90	*SHH*
ENSG00000171401	2166.124	11.253	0.771	3.18E-48	2.88E-45	*KRT13*
ENSG00000164458	17720.383	11.250	0.904	1.40E-35	6.25E-33	*TBXT*
ENSG00000188991	437.437	10.888	0.510	3.36E-101	2.37E-97	*SLC15A5*
ENSG00000169676	132.857	10.409	0.854	3.75E-34	1.44E-31	*DRD5*
ENSG00000171345	65725.635	10.391	0.677	3.95E-53	4.23E-50	*KRT19*
ENSG00000124143	1036.153	10.221	0.437	6.43E-121	1.14E-116	*ARHGAP40*
ENSG00000181072	4607.207	10.086	0.788	1.75E-37	9.25E-35	*CHRM2*
ENSG00000179817	84.678	9.962	0.577	1.02E-66	2.11E-63	*MRGPRX4*
ENSG00000204121	60.801	9.856	0.880	4.09E-29	1.06E-26	*ECEL1P1*
ENSG00000173826	526.286	9.438	0.540	2.12E-68	5.00E-65	*KCNH6*
ENSG00000119125	4881.511	9.364	0.702	1.23E-40	9.44E-38	*GDA*
ENSG00000114455	466.314	9.320	0.718	1.59E-38	9.70E-36	*HHLA2*
ENSG00000198074	6231.892	9.010	0.557	8.58E-59	1.17E-55	*AKR1B10*
ENSG00000226780	45.299	8.755	0.737	1.43E-32	5.09E-30	*AVPR1B-DT*
ENSG00000234575	31.556	8.685	0.731	1.54E-32	5.42E-30	*CTSLP8*
ENSG00000249321	24.907	8.643	1.463	3.45E-09	7.12E-08	*OR5H5P*
ENSG00000136155	242.893	8.597	0.785	6.88E-28	1.68E-25	*SCEL*
ENSG00000165370	281.602	8.542	0.717	1.06E-32	3.82E-30	*GPR101*
ENSG00000232743	23.905	8.509	0.819	2.70E-25	5.42E-23	*ELF2P3*
ENSG00000234828	155.860	8.457	0.540	2.98E-55	3.51E-52	*IQCM*
ENSG00000198049	493.355	8.338	0.715	1.92E-31	5.91E-29	*AVPR1B*
ENSG00000163283	38.792	8.336	0.819	2.33E-24	4.36E-22	*ALPP*
ENSG00000169213	25483.930	8.241	0.492	4.61E-63	7.08E-60	*RAB3B*
ENSG00000160349	343.761	8.187	0.640	1.64E-37	8.84E-35	*LCN1*
ENSG00000086548	152.373	8.167	0.927	1.27E-18	1.25E-16	*CEACAM6*
ENSG00000170465	40.049	7.991	0.879	9.47E-20	1.05E-17	*KRT6C*
ENSG00000288638	4954.332	7.900	0.979	6.84E-16	4.68E-14	*LNCDAT*
ENSG00000253649	1988.727	7.888	0.609	2.07E-38	1.24E-35	*PRSS51*
ENSG00000022355	602.661	7.875	1.135	3.91E-12	1.48E-10	*GABRA1*
ENSG00000232803	58.235	7.869	0.838	5.91E-21	7.80E-19	*SLCO4A1-AS1*
ENSG00000183313	26.541	7.747	0.630	9.52E-35	3.90E-32	*OR52L1*
ENSG00000140835	786.989	7.746	0.845	4.89E-20	5.64E-18	*CHST4*
ENSG00000170421	50290.655	7.732	0.585	7.32E-40	5.07E-37	*KRT8*
ENSG00000250221	31.502	7.658	0.609	2.65E-36	1.30E-33	*KRT8P32*
ENSG00000267799	170.913	7.584	1.165	7.46E-11	2.19E-09	*MAN1A2P1*
ENSG00000239481	22.398	7.337	0.646	7.36E-30	2.00E-27	*RPS3AP41*

Supplemental table 4. *Continued*

ensembl_gene_id	baseMean	log2FoldChange	lfcSE	pvalue	FDR	hgnc_ symbol
ENSG00000134765	135.712	7.334	0.619	2.09E-32	7.32E-30	*DSC1*
ENSG00000100884	40.981	7.289	0.879	1.11E-16	8.29E-15	*CPNE6*
ENSG00000150625	1648.761	7.287	0.579	2.42E-36	1.21E-33	*GPM6A*
ENSG00000265190	738.169	7.286	0.497	1.09E-48	1.04E-45	*ANXA8*
ENSG00000088836	8496.681	7.263	0.468	2.66E-54	2.94E-51	*SLC4A11*
ENSG00000215372	58.235	7.230	0.968	8.15E-14	4.08E-12	*ZNF705G*
ENSG00000250821	124.316	7.208	0.825	2.41E-18	2.29E-16	*EXOC1L*
ENSG00000258628	34.327	7.110	0.740	6.97E-22	1.01E-19	*RHPN2P1*
ENSG00000116983	1096.094	7.058	0.571	4.29E-35	1.85E-32	*HPCAL4*
ENSG00000164007	125.465	7.017	1.036	1.28E-11	4.42E-10	*CLDN19*
ENSG00000149948	694.337	-5.613	0.616	8.29E-20	9.36E-18	*HMGA2*
ENSG00000112280	18140.111	-5.660	1.112	3.56E-07	4.61E-06	*COL9A1*
ENSG00000106278	486.527	-5.681	0.833	9.11E-12	3.25E-10	*PTPRZ1*
ENSG00000221867	137.788	-5.702	1.840	0.001946272	0.008201037	*MAGEA3*
ENSG00000214249	25.536	-5.705	0.911	3.76E-10	9.55E-09	*CTAGE11P*
ENSG00000228035	99.583	-5.830	1.016	9.71E-09	1.81E-07	*NGF-AS1*
ENSG00000130829	64.427	-5.866	1.090	7.31E-08	1.11E-06	*DUSP9*
ENSG00000163501	174.541	-5.912	0.765	1.12E-14	6.58E-13	*IHH*
ENSG00000204941	100.853	-5.947	1.623	0.000248902	0.001424626	*PSG5*
ENSG00000135903	334.212	-5.965	0.950	3.37E-10	8.67E-09	*PAX3*
ENSG00000047936	387.764	-6.007	0.896	1.99E-11	6.54E-10	*ROS1*
ENSG00000116690	7782.709	-6.017	0.824	2.90E-13	1.33E-11	*PRG4*
ENSG00000280650	20.970	-6.053	0.986	8.15E-10	1.93E-08	*KCNIP4-IT1*
ENSG00000147655	872.328	-6.078	0.931	6.60E-11	1.96E-09	*RSPO2*
ENSG00000228536	89.798	-6.085	0.727	5.93E-17	4.56E-15	*LYPLAL1-AS1*
ENSG00000206384	250.052	-6.127	1.054	6.11E-09	1.19E-07	*COL6A6*
ENSG00000187268	78.162	-6.201	0.925	2.03E-11	6.65E-10	*FAM9C*
ENSG00000185306	80.711	-6.292	0.824	2.31E-14	1.29E-12	*C12orf56*
ENSG00000002745	182.223	-6.318	0.984	1.35E-10	3.80E-09	*WNT16*
ENSG00000000005	181.441	-6.344	1.005	2.78E-10	7.31E-09	*TNMD*
ENSG00000223949	392.693	-6.419	0.818	4.09E-15	2.53E-13	*ROR1-AS1*
ENSG00000255399	137.995	-6.561	0.775	2.48E-17	2.05E-15	*TBX5-AS1*
ENSG00000128714	139.859	-6.612	0.828	1.35E-15	8.81E-14	*HOXD13*
ENSG00000224963	321.758	-6.694	0.874	1.91E-14	1.08E-12	*ECMXP*
ENSG00000019186	155.754	-6.710	1.129	2.79E-09	5.86E-08	*CYP24A1*
ENSG00000127743	328.669	-6.710	0.986	1.02E-11	3.59E-10	*IL17B*
ENSG00000197587	26.489	-6.711	1.050	1.67E-10	4.60E-09	*DMBX1*
ENSG00000237396	58.068	-6.854	1.820	0.000165895	0.001008677	*LNCNEF*
ENSG00000072041	328.019	-6.885	1.132	1.19E-09	2.73E-08	*SLC6A15*
ENSG00000016082	26.411	-6.893	0.988	3.07E-12	1.19E-10	*ISL1*
ENSG00000166509	2186.658	-7.063	1.645	1.75E-05	0.000143606	*CLEC3A*
ENSG00000162624	45.059	-7.081	1.291	4.17E-08	6.73E-07	*LHX8*
ENSG00000206013	448.828	-7.096	1.608	1.02E-05	8.94E-05	*IFITM5*
ENSG00000144191	36.932	-7.174	1.539	3.12E-06	3.15E-05	*CNGA3*
ENSG00000137745	8572.135	-7.207	0.861	5.60E-17	4.34E-15	*MMP13*
ENSG00000244681	97.039	-7.332	1.543	2.03E-06	2.15E-05	*MTHFD2P1*
ENSG00000107984	1704.251	-7.416	0.710	1.57E-25	3.24E-23	*DKK1*

Supplemental table 4. *Continued*

ensembl_gene_id	baseMean	log2FoldChange	lfcSE	pvalue	FDR	hgnc_ symbol
ENSG00000154143	459.193	-7.440	1.727	1.65E-05	0.000136125	*PANX3*
ENSG00000080224	566.494	-7.472	0.889	4.14E-17	3.26E-15	*EPHA6*
ENSG00000089225	114.537	-7.771	0.894	3.56E-18	3.30E-16	*TBX5*
ENSG00000164488	235.562	-7.804	1.256	5.28E-10	1.30E-08	*DACT2*
ENSG00000180318	88.989	-7.854	1.241	2.43E-10	6.47E-09	*ALX1*
ENSG00000254254	132.585	-8.081	1.123	6.20E-13	2.72E-11	*PENK-AS1*
ENSG00000164825	91.444	-8.248	1.219	1.31E-11	4.52E-10	*DEFB1*
ENSG00000185559	1362.438	-8.496	1.277	2.86E-11	9.05E-10	*DLK1*
ENSG00000136110	4485.869	-9.831	1.808	5.43E-08	8.51E-07	*CNMD*
ENSG00000182674	96.510	-9.833	1.286	2.08E-14	1.17E-12	*KCNB2*
ENSG00000181195	14343.109	-9.836	1.003	1.02E-22	1.61E-20	*PENK*
ENSG00000187689	31.002	-24.008	2.727	1.34E-18	1.31E-16	*AMTN*
ENSG00000185960	40.413	-24.343	1.455	8.36E-63	1.23E-59	*SHOX*

Supplemental table 5. Univariate cox proportional hazard results in the combined cohort. Table includes the results of the disease-specific survival in association with all identified T cell phenotypes. Log-rank P values < 0.05 were considered significant. * < 0 .05, ** < 0.01, *** < 0.001. HR = hazard ratio; CI = confidence interval.

	Disease-specific survival	
	Univariate	
Variable	**HR (95% CI)**	**log-rank P**
Ki-67$^+$CD4$^+$ T cells	0.93 (0.72-1.2)	0.6
Ki-67$^+$CD8$^+$ T cells	1 (0.9-1.1)	0.9
Ki-67$^+$ Regulatory T cells	0.8 (0.46-1.4)	0.4
CD4$^+$ T cells	1 (0.99-1)	0.5
CD8$^+$ T cells	1 (0.98-1.01)	0.8
Regulatory T cells	0.95 (0.88-1.02)	0.2

Supplemental table 6. Univariate and multivariate cox proportional hazard results in the combined cohort. Table includes the results of the disease-specific, recurrence-free and metastasis-free survival. Significant parameters from the univariate analysis were taken along for the multivariable analysis. Patients who were only treated with radiotherapy were excluded from the recurrence-free survival analysis. Log-rank P values < 0.05 were considered significant and are annotated in bold and by significance level; * < 0 .05, ** < 0.01, *** < 0.001. HR = hazard ratio; CI = confidence interval; RT = radiotherapy.

Disease-specific survival	Univariate	
Variable	**HR (95% CI)**	**log-rank *P***
Age at diagnosis	1 (0.98-0.99)	0.2
Max tumour size	1 (0.91-1.2)	0.7
Location (Skull base)[a]		
Mobile Spine	0.56 (0.2-1.6)	0.09
Sacrococcygeal	0.35 (0.13-0.92)	
Treatment (RT alone)		
Surgery	0.87 (0.24-3.1)	0.6
Surgery + RT	0.57 (0.15-2.2) *	
Timing of RT (Adjuvant)[b]		
Neoadjuvant	0.66 (0.076-5.8)	0.7
Surgical margin (R0)[c]		
R1	2.1 (0.23-19)	0.3
R2	2.3 (0.75-6.8)	
T cell infiltration (High)		
Low	2 (0.78-5.3)	0.1
Disease recurrence (No)[c]		
Yes	2 (0.78-5.3)	0.9

Metastasis-free survival	Univariate	
Variable	**HR (95% CI)**	**log-rank *P***
Age at diagnosis	1 (0.99-1)	0.3
Max tumour size	1.1 (0.95-1.2)	0.3
Location (Skull base)[a]		
Mobile Spine	0.84 (0.21-3.4)	0.8
Sacrococcygeal	1.2 (0.4-4)	
Treatment (RT alone)		
Surgery	1 (0.23-5.1)	1
Surgery + RT	0.95 (0.2-4.5)	

Supplemental table 6. *Continued*

Metastasis-free survival		Univariate
Timing of RT (Adjuvant)[b]		
Neoadjuvant	3.6e-9 (0-Inf)	0.2
Surgical margin (R0)		
R1	2.6 (0.29-23)	0.4
R2	0.68 (0.25-1.9)	
T cell infiltration (High)		
Low	1.5 (0.52-4)	0.5
Disease recurrence (No)[c]		
Yes	6.3 (0.83-48)	**0.04 ***

Recurrence-free survival[c]	Univariate		Multivariate	
Variable	**HR (95% CI)**	**log-rank *P***	**HR (95% CI)**	**log-rank *P***
Age at diagnosis	1 (0.98-1.02)	0.8		
Max tumour size	0.99 (0.9-1.1)	0.9		
Location (Skull base)[a]				
Mobile Spine	1.95 (0.94-4.02)	**0.003 ****	**2.2 (1-4.5) ***	
Sacrococcygeal	0.57 (0.26-1.2)		0.81 (0.32-2.1)	
Treatment (Surgery alone)				
Surgery + RT	0.82 (0.45-1.5)	0.5		0.01 *
Timing of RT (Adjuvant)[b]				
Neoadjuvant	0.29 (0.066-1.3)	0.08		
Surgical margin (R0)				
R1	1.6 (0.34-7.4)	0.07	1.2 (0.24-5.6)	
R2	**2.3 (1.1-4.8) ***		1.7 (0.7-4.2)	
T cell infiltration (High)				
Low	1.1 (0.6-2.1)	0.7		

[a]excluding the only patient with an extra-axial chordoma; [b]excluding patients who received a sandwich regimen of radiotherapy or radiotherapy alone; [c]excluding patients who were only treated with radiotherapy

SUPPLEMENTAL REFERENCES

1. Bertucci F, Finetti P, Simeone I, Hendrickx W, Wang E, Marincola FM, et al. The immunologic constant of rejection classification refines the prognostic value of conventional prognostic signatures in breast cancer. Br J Cancer. 2018;119(11):1383-91.
2. Ijsselsteijn ME, van der Breggen R, Sarasqueta AF, Koning F, de Miranda NFCC. A 40-Marker Panel for High Dimensional Characterization of Cancer Immune Microenvironments by Imaging Mass Cytometry. Front Immunol. 2019;10.
3. Somarakis A, Van Unen V, Koning F, Lelieveldt B, Hollt T. ImaCytE: Visual Exploration of Cellular Micro-Environments for Imaging Mass Cytometry Data. IEEE Trans Vis Comput Graph. 2021;27(1):98-110.
4. Nelson AC, Pillay N, Henderson S, Presneau N, Tirabosco R, Halai D, et al. An integrated functional genomics approach identifies the regulatory network directed by brachyury (T) in chordoma. J Pathol. 2012;228(3):274-85.
5. Duan W, Zhang B, Li X, Chen W, Jia S, Xin Z, et al. Single-cell transcriptome profiling reveals intra-tumoral heterogeneity in human chordomas. Cancer Immunol Immunother. 2022;71(9):2185-95.
6. Zhang Q, Fei L, Han R, Huang R, Wang Y, Chen H, et al. Single-cell transcriptome reveals cellular hierarchies and guides p-EMT-targeted trial in skull base chordoma. Cell Discov. 2022;8(1):94.